Project No. 09-831

Non-Destructive Thermal Analysis and In Situ Investigation of Creep Mechanism of Graphite and Ceramic Composites Using Phase-Sensitive THz Imaging & Nonlinear Resonant Ultrasonic Spectroscopy

Reactor Concepts RD&D

Dr. Xi-Cheng Zhang
University of Rochester

In collaboration with:
Idaho National Laboratory

David Hurley, Technical POC
Brian Robinson, Federal POC

NEUP Nuclear Energy University Programs
U.S. Department of Energy

Non-Destructive Thermal Analysis and In Situ Investigation of Creep Mechanism of Graphite and Ceramic Composites Using Phase-Sensitive THz Imaging & Nonlinear Resonant Ultrasonic Spectroscopy

Final Report

Contract No. DE-AC07-05ID14517
Subcontract No. 89653
Project No: 09-831

Technical Points of Contact and Principal Investigator:
Prof. Xi-Cheng Zhang
Institute of Optics, University of Rochester,
275 Hutchison Rd. Rochester, NY 14627-0186

Collaborator:
Dr. David H. Hurley
Science and Technology, Idaho National Laboratory,
1765 North Yellowstone Hwy. Idaho Falls, ID 83415

Albert Redo-Scanchez
Zomega Terahertz Corporation
15 Tech Valley Dr Suite 102. East Greenbush, NY 12061

Student:
Jing Zhang

October 2012

CONTENTS

LIST OF FIGURES

LIST OF TABLES

ABSTRACT

In this project, we conducted a comprehensive study on nuclear graphite properties with terahertz (THz) imaging. Graphite samples from Idaho National Laboratory were carefully imaged by continuous wave (CW) THz. The CW THz imaging of graphite shows that the samples from different billet with different fabricating conditions have different pore size and structure. Based on this result, we then used a phase sensitive THz system to study the graphite properties. In this exploration, various graphite were studied. By imaging nuclear graphite samples in reflection mode at nine different incident polarization angles using THz time-domain-spectroscopy, we find that different domain distributions and levels of porosity will introduce polarization dependence in THz reflectivity. Sample with higher density is less porous and has a smaller average domain distribution. As a consequence, it is less polarization-dependent and the polarization-dependent frequency is higher. The results also show that samples oxidized at higher temperatures tend to be more polarization dependent. The graphite from the external billet is more polarization dependent compared to that from the center billet. In addition, we performed laser-based ultrasonic measurements on these graphite samples. The denser, unoxidized samples allow surface acoustic waves to propagate more rapidly than in the samples that had already undergone oxidation. Therefore, for the oxidized samples, the denser samples show less polarization-dependence, higher polarization-dependent frequency, and allow the surface acoustic waves propagate faster.

I. INTRODUCTION

The Next Generation Nuclear Plant (NGNP) will be a high temperature gas-cooled reactor (HTGR) with a large graphite core. Graphite has been established as a viable structural material and neutron moderator for HTGRs, permanent side reflectors, and for the core support structure. However, the previous graphite grade qualified for nuclear service, H-451, is no longer available. Furthermore, the present understanding of graphite behavior of H-451 is not sufficient enough to be extrapolated to new nuclear graphite grades. New grades must therefore be fabricated, characterized, and irradiated to meet the performance requirements of the NGNP [1].

There are several concerns in qualifying new grades of graphite. It would be highly desirable to gain a robust fundamental understanding of irradiated graphite behavior to ensure new theories and models that could predict graphite behavior during the lifetime of the reactor. Thus the operators will have data and understanding for decisions on replacement timing of changing cores, components, and structures. To the extent that this is achieved, it would provide more confidence for design and licensing and reduce the experimental verification for new graphite grades. Because of the inherent variability of the physical, mechanical, and thermal properties for a given graphite grade within a billet, between billets and between lots, a good understanding of this variability is needed to establish behavioral models of (degradation) phenomena during reactor life. Moreover, the effects of reactor environment (temperature, neutron irradiation, and chemical attack) on the physical properties of graphite must be clarified. Finally, for different types of graphite, the irradiation-induced dimensional change that drives the generation of graphite component stresses, and irradiation creep behavior that relieves graphite component stresses must be determined over a representative temperature and fluence range [2].

In this exploration, we studied the variability of microstructure properties of nuclear-grade graphite using continuous wave (CW) terahertz (THz) imaging, phase-sensitive THz imaging and nonlinear laser-based resonant ultrasound techniques. These are non-destructive evaluation techniques that will be used to monitor the mechanical properties of graphite, including the size, distribution, shape and orientation of both pores and grains. Initially, measurements were made on surrogate samples subjected to weight loss due to oxidation. Ex-situ examinations were conducted to monitor pore distribution and size as well as crack distribution and size. Ultimately, these baseline measurements will be used to design and implement in-situ experiments to monitor pore and crack evolution as well as crystal texture evolution. The results of this study will be used to support new multi-scale model development, which will make contributions to the fundamental understanding of irradiation creep.

II. BACK GROUND

A. NUCLEAR GRAPHITE

Nuclear-grade graphite is a composite material made from petroleum or a coal-tar-based coke and a pitch binder. Manufacturing graphite is an iterative process of baking and pitch impregnation of a formed billet at temperatures greater than 2500 ℃. Integral to this process are the use of isotropic cokes and a special forming process (i.e., isostatically molded, vibrationally molded, or extruded) which are intended to obtain an isotropic or near isotropic graphite.

However, the source, size, and blend of the original materials as well as the forming process of the green billet will impact material properties as well as variations within the final product. There will be density variations from the billet surface inward and different physical properties with and transverse the forming direction, which are expected within individual billets as well as billet-to-billet and lot-to-lot. Other manufacturing defects include large pores, inclusions, and cracks. In addition to the material variation inherent to the manufacturing process, graphite will experience changes in physical properties while in service in a nuclear reactor, accompanied by the possibility of cracking due to stress and oxidation resulting from constituents in the gas coolant or oxygen ingress. Therefore, it is necessary to nondestructively characterize a variety of material attributes such as uniformity, isotropy, and porosity as a method to assure consistent stock material. It is also necessary to detect isolated defects such as cracks, large pores and inclusions, or distributed material damage such as micro-cracking and material loss due to oxidation.

B. THZ IMAGING

Terahertz (THz) waves, which occupy a portion of the electromagnetic spectrum (0.1 - 10 THz) between the infrared and microwave regime, offer innovative imaging and sensing technologies which provide information not available through conventional methods, such as microwave and X-ray techniques [3]. THz imaging has many advantageous features. It is non-destructive and can be generated and detected remotely which enables monitoring of material properties in harsh environments (e.g. high temperature and high dose neutron radiation). THz waves can penetrate most nonmetal materials and yet are non-ionizing, unlike X-rays. Therefore, THz imaging offers the capability of identifying internal damage or cracks without any external damage/ionization. Furthermore, THz waves are polarized and can provide anisotropic information through THz imaging. These unique features make THz imaging a powerful technique to characterize new grades of graphite. Fig. 1 illustrates a typical THz imaging system in reflection and tomographic mode.

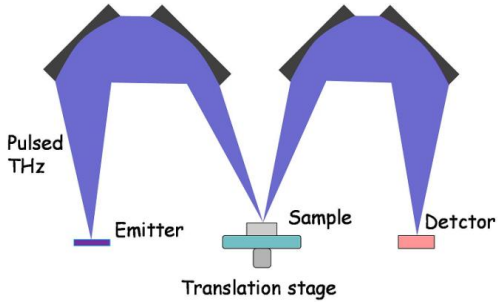

Fig. 1. Schematic setup for THz imaging.

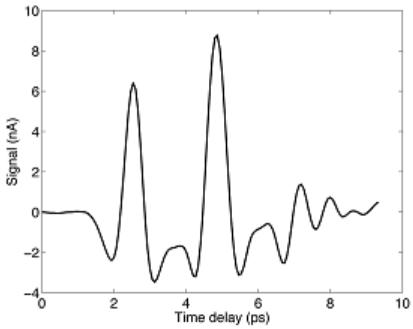

Fig. 2. Time domain waveform of damaged graphite composite. Multiple peaks correspond to delamination.

Our previous work on graphite composite materials for characterizing fire damage has demonstrated that THz techniques have the potential to investigate the damage induced by the environmental changes. In these cases, the damage to graphite composites led to either fiber re-orientation or a chemical change causing a change in the electrical conductivity. The reflectivity of the samples was measured to be anisotropic and depended on the polarization of the applied THz waves. The change in the polarization-sensitive reflectivity indicated damage in the graphite sample and this change manifested as high and low contrast regions in the THz image. Any deformation or delamination in the graphite leads to change in the time-domain waveform obtained by THz spectrometer. Furthermore any discontinuity inside the sample from cracks or change of properties can be resolved as well, making THz tomographic imaging possible. Fig. 2 shows a 1D tomography curve from graphite composite, where layered structures can be identified. Fig. 3 shows both

optical and THz images of burnt graphite fiber composite with THz images showing higher contrast and providing anisotropic information.

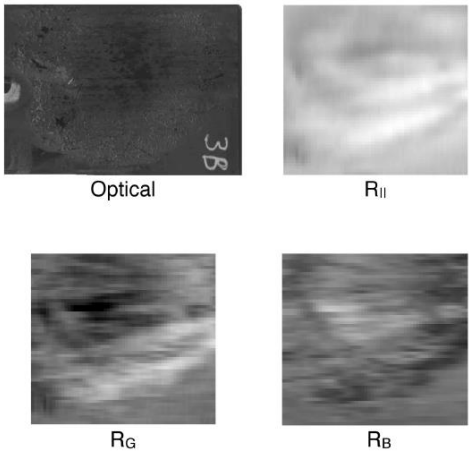

Fig. 3. Images of graphite fiber composite with severe burn damage (area: 28x31 mm^2). $R_{\parallel}$ is obtained with the THz wave polarized parallel to the fibers of the material, resulting in the highest reflectivity. R_G is the polarization- sensitive reflectivity of the grid of wires and R_B is the background reflectivity and equal to the reflectivity obtained when the polarization of the THz wave is perpendicular to the fibers.

C. LASER-BASED RESONANT ULTRASOUND SPECTROSCOPY

Resonant ultrasound spectroscopy (RUS) involves the study of the mechanical resonances of solids [4-7]. The resonant response of a particular object depends on the shape, elastic constants, mechanical texture, and porosity. Any and all of these properties can change for samples exposed to creep environments. In order to monitor microstructure evolution *in situ*, it is important that the ultrasonic transduction method be amenable to use in high temperature environments. Laser ultrasound is a particularly appealing transduction method for such situations. Acoustic generation is accomplished by irradiating a specimen with a short pulse (~10ns) from a high-intensity laser. The absorbed optical energy is quickly (~100 fs) converted into a steep thermal gradient which, through the action of thermal expansion, creates an acoustic wave. A laser interferometer is used to detect ultrasonic waves by sensing small, ultrasonically-induced changes in optical phase. At the national laboratory, we have developed a robust, materials characterization technique by combining elements of laser ultrasonic and resonant ultrasound spectroscopy. This technique known as laser-based RUS (LRUS) [8], has proven to be particularly well suited for *in-situ* characterization of mechanical properties.

Analysis of the nonlinear ultrasonic response of a material offers the potential for measuring certain material properties more effectively than techniques that assume linear behavior. To establish a baseline, nonlinear laser-based resonant ultrasound spectroscopy (NLRUS) was performed on an annealed, fully dense copper (Cu) sample. These results were contrasted with the same measurements performed on a nickel alloy sample exposed to a creep fatigue environment. The top series of images in Fig. 4 shows the results for the Cu sample. The decrease in peak frequency with increasing ultrasound amplitude is due to crystal nonlinearity. This type of nonlinearity is present in all materials and stems from the non-parabolic binding energy curve. The bottom series of images in Fig. 4 shows the results for the nickel alloy sample. In this case, the behavior as a function of increasing ultrasonic amplitude is markedly different from the Cu sample. The peak not only shifts to lower frequency but also splits into three distinct peaks (due to nonlinear mixing with lower frequency peaks). The origin of the nonlinear behavior is due to the presence of micron-order fatigue cracks. The cracks act as

mechanical rectifiers – passing the compression part of the ultrasonic wave and reflecting the tension part of the ultrasonic wave.

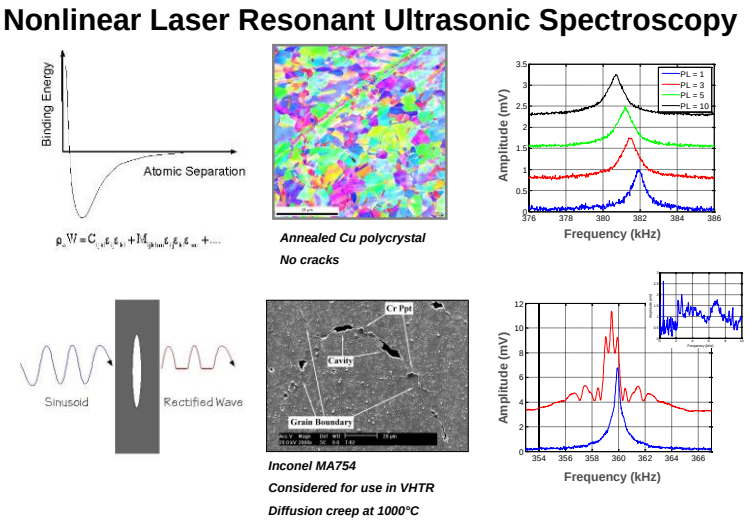

Fig. 4. Top: Laser-based nonlinear resonant ultrasound investigation of fully dense copper (Cu). The shift in the resonant peak with increasing ultrasonic amplitude is due to crystal nonlinearity. Bottom: LRUS investigation of a nickel alloy exposed to a creep-fatigue environment. Peak splitting is due to nonlinear mixing with lower frequency peaks.

III. SAMPLE INFORMATION

Table 1. Properties of tested graphite types

Sample	T_{max} (℃)	Density (kg/m^3)		
		Initial	Post	Current
A44	600	1770.6	1503.3	1500.8
A21	650	1766.7	1417.3	1407.2
B08	Unoxidized			1798.9
B38	600	1804.4	1522.2	1520.9
B18	650	1806.1	1474.1	1469.1
C52	Unoxidized			1821.8
C23	600	1836.4	1494.3	1490.6
C58	650	1831.8	1455.9	1438.9
H-451, #9	600	1770.8	1504.3	1499.5
H-451, #8	650	1839.5	1558.4	1538.8
H-451, #7	700	1767.0	1494.7	1437.2
SPI-2	Unoxidized			2270.0

Measurements were made on four types of nuclear grade graphite. Sample series A is a gas-purified, molded graphite (PGXW) supplied by GrafTech International. Series B is an extruded graphite (NBG-10) supplied by SGL Carbon Group. Series C is a specialty graphite (R4-650) also supplied by SGL Carbon. Series H-451 is an extruded, medium grained, nearly isotropic graphite. SPI-2 is a highly ordered pyrolytic graphite (HOPG) ordered from SPI, which exhibits a mosaic angle as small as 0.8 ° +/- 0.2. See Table 1for data on the five

material types. As shown in Table 1, these samples were either unoxidized or thermally oxidized to 600 ℃, 650 ℃ or 700 ℃. The photos of the nuclear graphite samples are shown in Fig. 5.

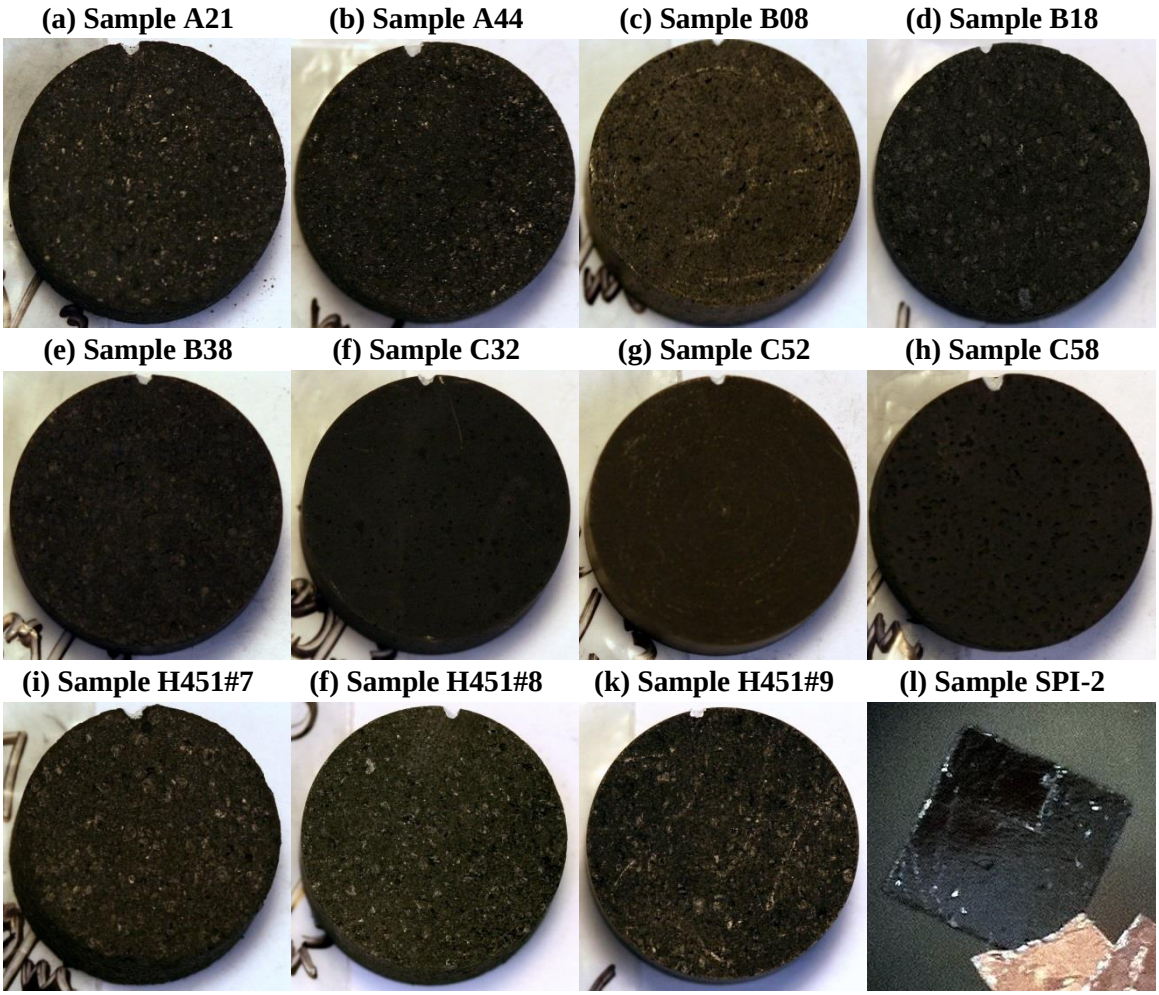

Fig. 5. Photos of all the nuclear graphite samples.

IV. PHASE SENSITIVE THZ IMAGING OF NUCLEAR GRAPHITE

A. SUMMARY

In this exploration, high order pyrolytic graphite (HOPG) was characterized using both transmission and reflection THz spectroscopy in a broadband range. Two different THz time-domain spectroscopy systems were used for the characterization of the samples: a conventional THz TDS system and an air-biased coherent detection (ABCD) THz spectroscopy system [9]. Strong birefringence is observed with different dielectric constants along three geometries. Each geometry is determined by the different combination of THz waves propagating direction, polarization direction and carbon layer direction. Lowest dielectric constants are obtained when THz waves propagate along the carbon plane direction and are polarized perpendicular to the plane. For transmission measurements, graphite samples with various thicknesses are prepared. THz waves are shown to be able to transmit through 200 microns of graphite under the third geometry, but not under the other geometries.

B. SAMPLE PREPARATION

The samples tested were purchased from graphitestore.com. The samples are pyrolytic graphite plate and not necessarily high order pyrolytic graphite (HOPG). Crystalline graphite is a layered compound. In each layer, the carbon atoms are arranged in a hexagonal lattice with separation of 0.142 nm, and the distance between planes is 0.335 nm. Graphite can conduct electricity due to the vast electron delocalization within the carbon layers (a phenomenon called aromaticity). These valence electrons are free to move, and are able to conduct electricity. However, the electricity is only conducted within the plane of the layers, not between layers. As a result, the conductivity and dielectric property of graphite is highly birefringent.

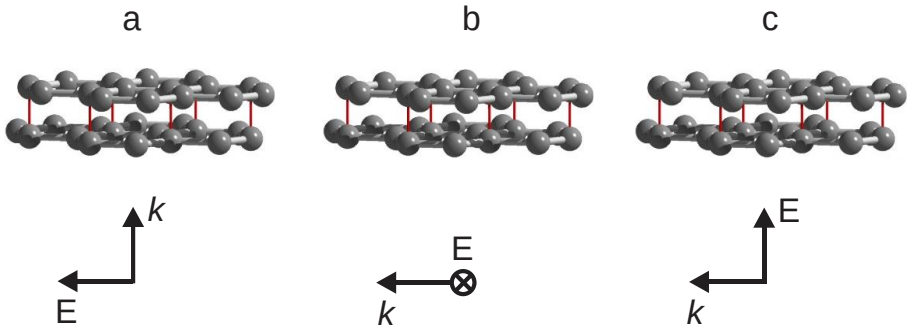

Fig. 6. (a) The first geometry, THz waves propagate perpendicular to the carbon layer and polarization lies inside the layers. (b) The second geometry, both of the THz waves propagate direction and THz polarization are parallel to the carbon layer. (c) The third geometry, THz waves propagate parallel to the carbon layer and polarization is perpendicular to the layer.

In order to study the THz properties of graphite, we measured THz reflection and transmission at three different geometries (orientations) as shown in Fig. 6. In the first geometry (Fig. 6(a)), THz waves propagate perpendicular to the carbon layer (i.e. along c axis), and THz polarization lies inside the carbon layer (perpendicular to c axis). In the second geometry (Fig. 6(b)), THz waves propagate parallel to the carbon layer, and THz polarization is also parallel to the carbon layer. In the third geometry (Fig. 6(c)), THz waves propagate parallel to the carbon layer, and THz polarization is perpendicular to the carbon layer.

The graphite plate was cut and polished into samples with a top area of 8 x 14 mm^2 with various thicknesses (1.5mm - 6mm). These samples are used in reflection measurement. However they are too thick for transmission measurement since almost all THz waves are absorbed by the thick sample and cannot go through. To achieve reasonable transmission, thin graphite samples are prepared with a thickness of 140 and 200 micron, respectively. Graphite samples are first glued to a high-resistivity silicon substrate, and then polished to the desired thickness. It is worthwhile to note that the polishing occurs in the direction that is perpendicular to c axis (parallel to the carbon layer), not along the c axis, because we intend to characterize the graphite using the third and second geometries. For the thickness approaching 200 microns, THz waves still cannot transmit under the first geometry.

C. EXPERIMENTS AND RESULTS

Two different THz time-domain spectroscopy systems were used for the characterization of the samples: a conventional THz TDS system for transmission and reflection measurement, and an air-biased coherent detection (ABCD) THz spectroscopy system for reflection measurement. The conventional THz TDS has a useful bandwidth up to 4 THz with a dynamic range of 70 dB. The available bandwidth of ABCD system spans from 0.1 THz to 15 THz with a slightly lower dynamic range. The THz pulse transmitted through

/reflected by the silicon substrate was used as reference and compared with the pulses transmitted/reflected from the samples.

C1. TRANSMISSION SPECTROSCOPY

Fig. 7. Photo of a THz TDS system without transmission module.

Fig. 7 shows the photo of a THz-TDS system without transmission module. It has a useful bandwidth up to 4 THz. In our measurement, a reference THz pulse was recorded with a silicon blank placed in the beam path. Then a sample on a silicon substrate was placed into THz beam path and the THz pulse was measured after transmission through the sample. For this measurement, the third geometry is employed, where THz waves propagate parallel to the carbon layer and THz polarization is perpendicular to the carbon layer. Other geometries do not allow THz transmission through these graphite samples. All measurements were performed in a nitrogen-purged environment. Fig. 8(a) shows the THz pulses of reference and after transmission through the samples. Fig. 8(b) shows the Fourier-transformed spectra after transmission through the silicon blank (reference) and the samples. Fig. 8(c) shows the relative transmission, which is defined as the ratio of transmission through the sample-on-substrate to the silicon blank.

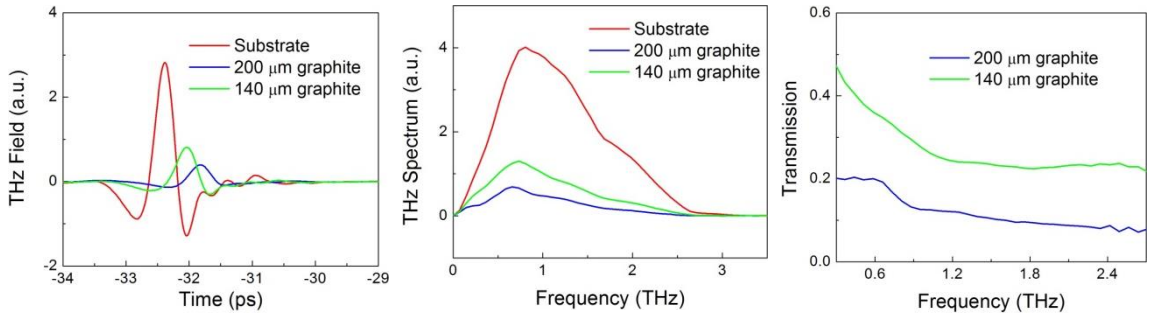

(a) (b) (c)

Fig. 8. (a) THz temporal waveforms for reference and after transmission through the samples. (b) THz spectra for reference and after transmission through the samples. (c) Relative transmission through the sample.

The time-of-flight between the pulse through the blank silicon and the pulses through the samples, observed in Fig. 8(a), is caused by the optical thickness of the thin graphite films. A quick estimation using the time

delay yields an average refractive index of 1.9 for graphite at THz frequency, in agreement with literature. Moreover, transmission is frequency-dependent, where low frequency has higher transmission, as seen in Fig. 8(c).

C2. REFLECTION SPECTROSCOPY

Standard System

Transmission measurements can only be obtained using the third geometry. Therefore, it becomes necessary to use reflection geometry to characterize the graphite in other orientations (geometries). First we use the mini-Z for reflection characterization of graphite along three different orientations in the frequency range of 0 - 3 THz. The advantage of the mini-Z is that it is portable and may be used for in-situ monitoring of graphite. Fig. 9 shows the reflected THz spectra and reflectance at three different geometries. As expected, strong birefringence is observed. In the first geometry, THz waves propagate along the c axis and are polarized inside the carbon plane. THz waves experience the strong dielectric constant, showing the highest reflectance. In addition, the reflection is independent of THz polarization inside the carbon plane. In the second geometry, THz waves also experience strong reflection, indicating large dielectric constants. In the third geometry, THz waves show dramatically different behavior with much lower reflectance. The reflectance is greatly reduced, indicating much smaller dielectric constants.

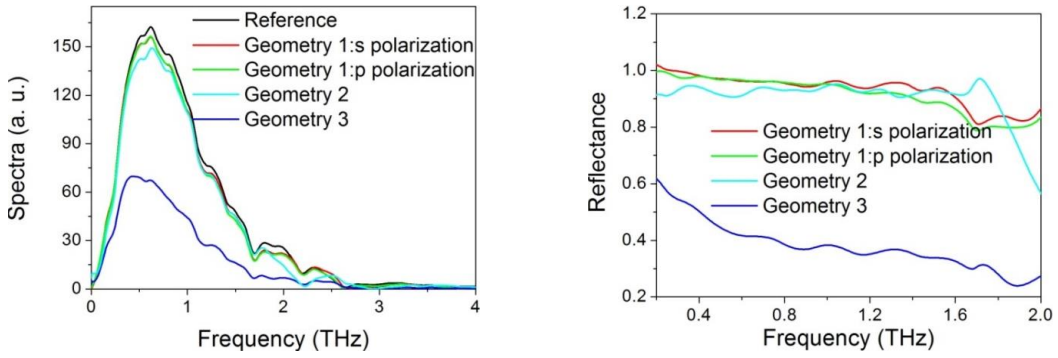

(a) (b)

Fig. 9. (a) Reflected THz spectra from graphite under different geometry. (b) Field reflectance from graphite under different geometry.

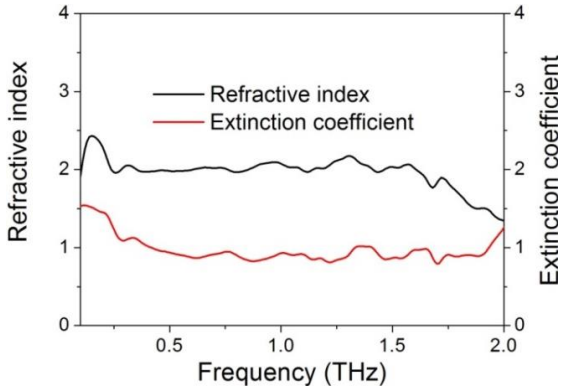

Fig. 10. Refractive index and extinction coefficient of graphite with the third geometry.

We can also derive refractive indexes and extinction coefficients from the reflection measurements. However, the index and coefficient values are inaccurate and unreliable when the reflectance approaches unity. As a result, we only show the values of indexes and coefficients for the third geometry, shown in Fig. 10. The values are in agreement with both literature and transmission measurement.

Ultrabroadband System

For broadband reflection measurement from 0 - 15 THz, an ABCD system is used. Details of the ABCD setup are shown in Table 2.

Table 2. Parameters of ABCD experimental setup.

Setup / System	ABCD normal incident system
Laser	SP Hurricane amplifier; 1 kHz, 800 mW; 100 fs
THz Emitter	Nitrogen purged
Biased Electric field [V]	~20kV/cm
THz Receiver	Nitrogen purged; fused silica lens
Modulation Frequency	500 Hz
Lock-In Time Constant	300 ms
Measurement Type	Normal transmission (incident angle 0^0)
Emitter parabolic mirror FL	3”
Detector parabolic mirror FL	2”
Beam splitter ratio	Pump and Probe 75:25
FL of lens in emitter part	150mm
FL of lens in detector part	125mm

Fig. 11(a) shows the THz pulses reflected from a silver mirror (reference) and from the samples with two different geometries and measured by ABCD THz spectroscopy system. Compare with conventional THz TDS, ABCD spectroscopy has much broader spectra and narrower temporal pulse.

In order to evaluate the broadband frequency-dependence of the THz property of graphite, we performed a Fourier transformation of the pulses to get their spectra, shown in Fig. 11(b). No signature is observed within the THz frequency range. Furthermore, strong birefringence is observed up to 10 THz. Fig. 11(c) shows the THz field reflectance from the sample for the three geometries. The first and second geometries indicate a large refractive index with reflectances close to 1. On the other hand, the third geometry indicates a much smaller refractive index with the reflectance between 0.3 and 0.4, and is in better agreement with the literature.

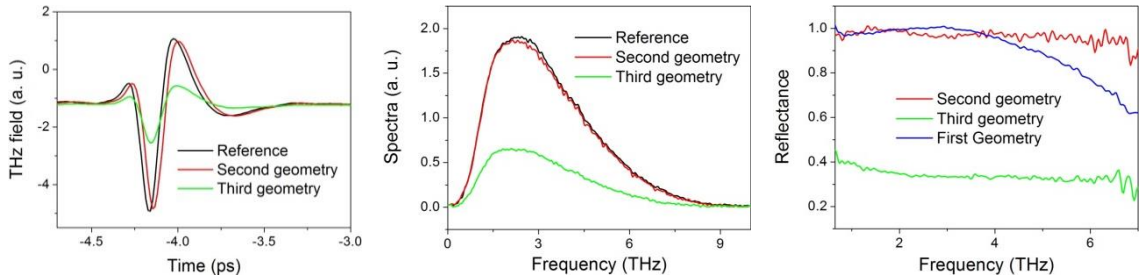

(a) (b) (c)

Fig. 11. (a) THz pulses reflected from a silver mirror (reference) and from graphite under the second and third geometry. (b) THz spectra of reference and reflected from the sample under two geometries. (c) Reflectance from the sample under three geometries.

D. CONLUSIONS AND DISCUSSIONS

- Pyrolytic graphite has been characterized using both transmission and reflection THz spectroscopy in a broadband range.
- Strong birefringence is observed with different dielectric constants along three geometries. Lowest dielectric constants are obtained when THz waves propagate along the carbon plane direction and are polarized perpendicular to the plane.
- For transmission measurements, graphite samples with various thicknesses are prepared. THz waves are shown to be able to transmit through 200 microns of graphite only under the third geometry, not under the other geometries.
- For THz imaging inside graphite, it will be necessary to employ the third geometry.

V. CW THZ IMAGING OF NUCLEAR GRAPHITE

A. SUMMARY

Graphite samples H-451#9, A44, B08 and C21 (from INL) were carefully imaged by a CW THz gas laser (SIFIR-50, Coherent Inc.) as a source and a pyroelectric sensor (PY55, Goodrich Co.) as a detector. The continuous wave (CW) imaging of the graphite samples indicates that the sample reflection depends on the THz polarization even if the propagation direction of the THz is not varied with respect to the carbon layer plane. The optical properties of the samples depend strongly on the complex refractive index of the material. The difference in the contrast and the features of the samples for two different orientations of the sample indicates that the material is anisotropic at THz frequencies. Furthermore, the samples from different categories show different structure and different contrast, indicating that the samples have different pore sizes and structures. This information will be used in further studies of the samples.

B. CW THZ IMAGING SYSTEM SETUP

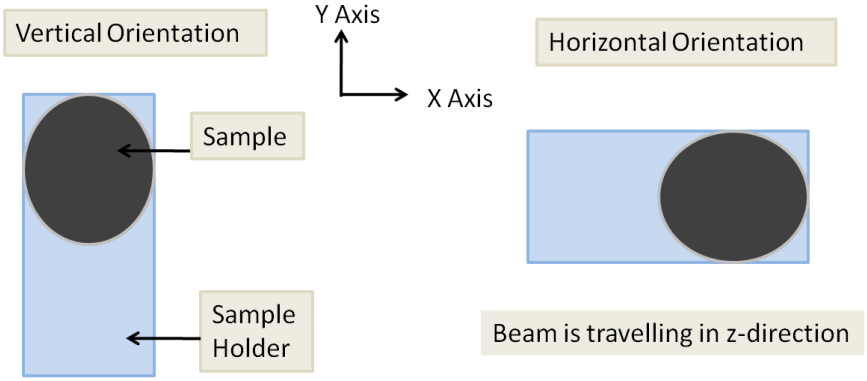

Fig. 12. Schematic describing the orientation of the samples used for the imaging.

A THz imaging system has been set up in normal incidence reflection geometry using a CW THz gas laser (SIFIR-50, Coherent Inc.) as a source and a pyroelectric sensor (PY55, Goodrich Co.) as a detector. The gas laser is able to operate at 11 different frequencies ranging from 1.01 THz to 7.6 THz. The frequency line corresponding to 1.63 THz provides the highest output power (180 mW) compared to other operating frequencies, therefore we operate here for this experiment. The system employs the raster scan method to obtain a 2-dimensional (2D) image and it takes almost 30 minutes to acquire one image. The imaging system

has a spatial resolution of around 0.3 mm and a SNR of 1000:1 and dynamic range of almost 40 dB. The resolution of the system is determined using the pyroelectric camera as well as using a resolution target. The signal from a pyrodetector is fed into a lock-in amplifier and the data is acquired by a computer using a Labview® program. For the image post-processing using Matlab®, an "unsharp mask" is applied to the raw data. This mask is used to sharpen the images. It does not create additional details rather it enhances the appearance of the details. Graphite samples H-451#9, A44, B08 and C21 (from INL) were carefully imaged at a step size of 250 microns. Two THz images were obtained for each sample: Initially at the original orientation, hereby called the vertical orientation and later after the sample was rotated by 90 degrees azimuthally, hereby called the horizontal orientation as shown in Fig. 12.

C. RESULTS AND DISCUSSTION

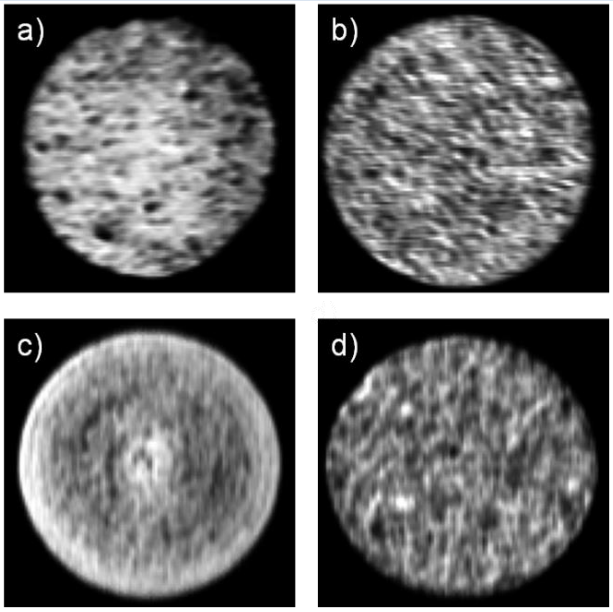

Fig. 13. CW THz images of the samples in the Horizontal orientation. a) Sample A44 oxidized at 600 ºC with current density of 1500.8 kg/m3, b) Un-oxidized Sample B08 with current density of 1798.9 kg/m3, c) Un-oxidized Sample C52 with current density of 1821.8 kg/m3, d) Sample H451#9 oxidized at 600 ºC with current density of 1499.5 kg/m3.

The A, B and C series samples are molded type, extruded type and specialty type graphite samples respectively, which have different densities and were exposed to different temperatures. The THz images for the horizontal as well as vertical orientation illustrate the differences in the different series samples. Fig. 13 indicates that there are clear differences between the oxidized and un-oxidized samples. Further, there exist differences among the un-oxidized samples of B-type and C-type series as indicated by Fig. 13 b) and c). These images demonstrate the difference in the porosity of the samples because the pores give rise to lower reflectivity and appear as low signal or dark spots in the images.

The images obtained for different orientations of the sample also indicate the differences in the images. Statistical analysis on the samples (obtained using Image J software) i.e. counting the number of dark spots in the image indicates differences in the total number of spots for samples as well for one orientation versus other. The number of dark spots was calculated using a certain threshold value and counting the number of points which have value lower than that threshold value. Table 3 indicates the total number of dark spots for each sample for both horizontal as well as vertical orientation.

Table 3. Total number of dark spots, which correspond to low reflection spots in the sample, for 4 different samples for two different orientations.

Sample	Horizontal Orientation	Vertical Orientation
A44	277	385
B08	651	764
C52	343	505
H451#9	411	434

VI. POLARIZATION DEPENDENT IMAGING OF NUCLEAR GRAPHITE

A. SUMMARY

In this exploration, each nuclear graphite sample was imaged at 9 different orientations with respect to the polarization of the mini-Z THz spectrometer to determine the polarization-dependent reflectivity. The results show that a sample with higher density is less porous and has a smaller average domain distribution. As a consequence, it is less polarization-dependent, whereas samples oxidized at higher temperatures tend to be more polarization dependent. In addition, sample from the center billet could be less polarization dependent compared with that from the external billet.

B. THEORY

The graphite samples are polycrystalline and show different levels of porosity (density) and domain distribution. Each domain may have a dominant orientation of the graphite layers. The working hypothesis to explain the polarization-dependent characteristic is related to the size and distribution of these domains and their porosity. This hypothesis assumes that a domain with a size comparable to the THz wavelength will have a different reflectivity based on the relative orientation between the dominant crystal orientation and the polarization of the incident THz radiation. The size and distribution of these domains could depend on their structural condition, as well as on the preparation process.

At the microscopic level, if the majority of graphite crystals have their layers oriented perpendicularly to the incident THz radiation, the overall roughness of the surface is small (smaller than the THz wavelength) and the surface of the domain behaves like a mirror, thus no polarization dependency reflectivity is expected. On the other hand, if the dominant orientation of the graphite planes is not perpendicular to the incident THz radiation, the edges of the graphite planes get exposed to the incident THz radiation. The surface of this domain may show a larger roughness that may cause more scattering and stronger polarization dependent reflectivity. For example, imagine a surface with a roughness that is periodic in one of the surface directions. This surface may behave like a grating for a polarized THz photon with a wavelength that matches the spatial period of the roughness.

The size, size-distribution, and orientation of the domains could explain the observed results. We would expect that samples with smaller domains might show a lower polarization-dependent frequency than samples with larger size domains. Furthermore, inspired from the metallurgy discipline, we would expect that structurally stronger samples would show small domain sizes (with a narrow size distribution) and also have a higher density. On the other hand, we would expect that a fragile sample would show larger domain size with broader distribution and lower density.

C. EXPERIMENTAL SETUP

Fig. 14. THz imaging system.

The experimental setup is shown in Fig. 14. We use a commercially available time-domain spectrometer (TDS), the mini-Z, manufactured and commercialized by Zomega Terahertz Corp, as a THz imaging system. The mini-Z is connected to an Aerotech XYZ stage to acquire images of the nuclear graphite according to different orientation angles. In our system, the XY stage conducts a raster scan, while the Z stage rotates the sample with respect to the polarization of THz radiation generated by the mini-Z. A THz polarizer is placed in front of the mini-Z to filter out minor off-axis field components.

For these measurements, the data acquisition frequency was 3 Hz. Six signal waveforms were averaged for each pixel of the sample. The frequency span used to analyze the data ranged from 0.1 to 1.40 THz, with a frequency resolution of 10 GHz, providing 141 sampling points.

Each sample was imaged at 9 different orientations with respect to the polarization of the mini-Z THz spectrometer. The orientations are 0, 30, 45, 60, 90, 120, 135, 150, and 180 degrees. The polarization direction of the mini-Z in the images (Fig. 15a) was 45 degrees, approximately. The imaging area was 28x28 mm, with a step-size of 0.5 mm. Each sample took 16 hours to complete the set of 9 images.

D. PROCESSING AND ANALYSIS

D1. PROCESSING SCRIPT

Data was processed with Matlab®. The main steps of the processing are:

1. Correction of the offset or interlace between alternate scanning lines due to the raster scans when acquiring the images.
2. Masking of data to reduce computation load. Not all pixels in the image contain information about the sample. For instance, some of them belong to the substrate. This process only considers the pixels in the imaging area that are relevant to the sample.

3. Compensate the rotation of each image so each pixel corresponds to the same spatial position.
4. Smoothing the images to reduce the effect of errors induced by the rotation compensation. Rounding errors in the compensated position may misplace the exact location of a pixel by 1 pixel. Therefore, the value of each pixel is re-calculated by taking the average of that pixel and its immediate 8 neighbors.
5. Fit a polarization-dependent reflection model for each pixel.
6. Statistical analysis of the fitting parameters to determine its significance. For every pixel, a t-test is performed on the fitting parameters to determine whether or not the extracted parameters are significantly different from 0 with a 95% confidence level.

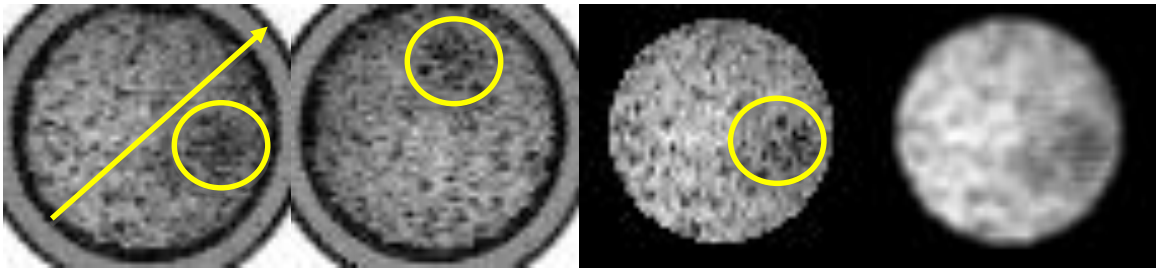

(a) (b) (c) (d)

Fig. 15. (a) A21 sample image at 0 degrees. The edges of the sample are used to fit a circle to determine the center of rotation. The polarization direction of the light emitted by mini-Z is 45 degrees (arrow). (b) Image of the same sample at 90 degrees orientation. (c) Previous image (b) compensated and trimmed. Only the pixels in the center are considered for analysis. (d) Result of smoothing image (c).

Fig. 15 shows an example of this processing on sample A21. The arrow indicates the polarization direction of the light emitted by the mini-Z. We can see a darker area (circled) and how this area's reflectivity changes as we rotate the sample. Fig. 15c shows the results of Fig. 15b after compensating for the sample rotation; thus, each pixel in Fig. 15a and Fig. 15c correspond to the same location. Fig. 15d is the result of smoothing Fig. 15c by averaging the value of each pixel with its immediate neighbors. This smoothing step is done to reduce the possible rounding errors caused by the compensation step.

D2. POLARIZATION REFLECTION MODEL

For each pixel, the reflected intensity is fitted as a function of the rotation angle. The polarization model used is described in Eq. (1).

$$R_{p,\nu}(\theta) = R_{p,\nu}^{(0)} + R_{p,\nu}^{(1)} \cos^2(\theta + \Phi) = \beta_{p,\nu}^{(1)} + \beta_{p,\nu}^{(2)} \cos(2\theta) + \beta_{p,\nu}^{(3)} \sin(2\theta) \quad (1)$$

Where θ is the rotation angle, $\beta^{(k)}$ are the fitting parameters for frequency ν and pixel p = (x,y), and $R(\theta)$ is the expected reflected intensity at frequency ν and pixel p. The equivalence between the fitting parameters and the model parameters is as follows:

$$R_{p,\nu}^{(0)} = \beta_{p,\nu}^{(1)} - \frac{1}{2} R_{p,\nu}^{(1)} \quad (2)$$

$$R_{p,\nu}^{(1)} = 2\sqrt{\left(\beta_{p,\nu}^{(2)}\right)^2 + \left(\beta_{p,\nu}^{(3)}\right)^2} \quad (3)$$

$$R_{p,\nu}^{(2)} = R_{p,\nu}^{(1)} \cos^2\left(\theta + \Phi\right) \tag{4}$$

$$\tan 2\Phi = \frac{-\beta_{p,\nu}^{(3)}}{\beta_{p,\nu}^{(2)}} \tag{5}$$

We will refer to $R^{(0)}$ as the non-polarization reflected intensity, which should be proportional to the reference intensity. $R^{(1)}$, $R^{(2)}$ and Φ are the reflected polarization-dependent intensity, reflected polarization intensity and polarization phase, respectively.

D3. STATISTICAL ANALYSIS

For each pixel $p = (x,y)$ and frequency ν, we have the $\beta^{(k)}$ and their standard deviation as the result of the fitting algorithm. Therefore, we can perform a t-test to determine whether $\beta^{(k)}$ is significantly different from zero at a certain confidence interval. In our case, we took a confidence level (CL) of 95%, which is common practice. The test assumes that two hypotheses exist, the null hypothesis (H_0) and the alternate hypothesis (H_1). In particular, in our case, the hypotheses are:

$$\begin{aligned} \mathrm{H}_0 &: \quad \beta_{p,\nu}^{(k)} = 0 \\ \mathrm{H}_1 &: \quad \beta_{p,\nu}^{(k)} \neq 0 \end{aligned} \tag{6}$$

The t-test provides the *t-value* and the *p-value*. The *p-value* is the probability under H_0 of obtaining a t-value that is greater than the value computed from the sample. If the *p-value* < (1 - CL), the null hypothesis is rejected.

In our case, the rejection of the null hypothesis means that the fitting parameter in question is significantly different from zero with a level of confidence of 95% and, therefore, the parameter should be considered as non-zero. Otherwise, the parameter can be considered to be equal to zero. In this report, we will refer to non-zero parameters as significant parameters.

D4. RESULTING DATASETS

For each sample, three sets of results are provided:

1. Fitting parameters significance count and overall r^2 coefficient or coefficient of determination (CoD). For each fitting parameter, the number of significant pixels is counted (pixels with non-zero significant parameters. The corresponding percentage of these significant pixels will give us an idea of the area of the sample that shows a polarization dependent reflection. The r^2 coefficient shown in the results section is computed as the average of the coefficient of determinations for all the pixels.
2. The average value of the fitting parameters $\beta^{(k)}$ and the extracted model parameters $R^{(0)}$, $R^{(1)}$, and Φ. These parameters will give us the relative strength of the polarization dependent behavior across the samples.

E. DENSITY AND OXIDIZE TEMPERATURE DEPENDENCE

E1. SAMPLE B08

Sample Images and Processed Images

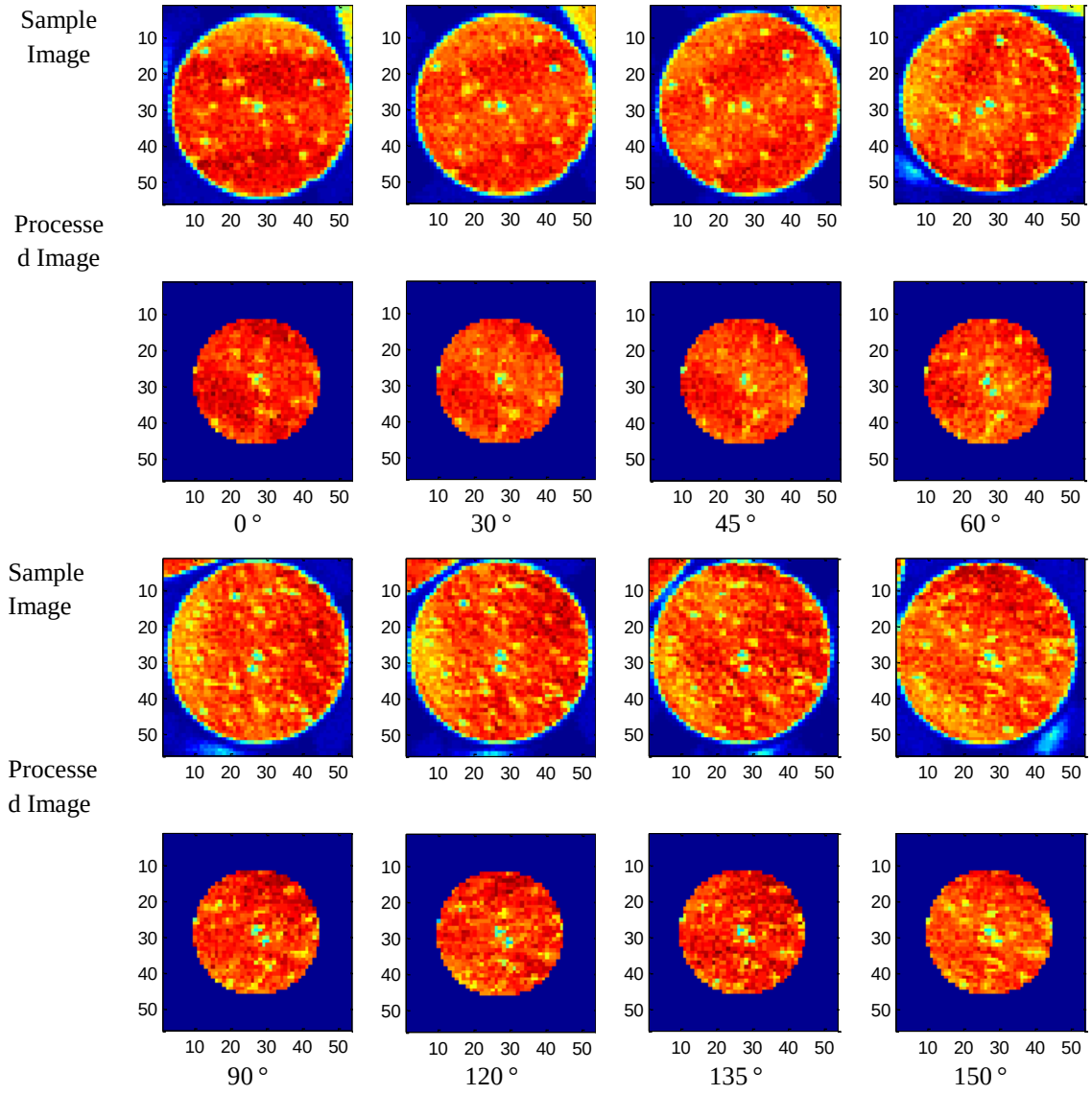

Fig. 16. Sample Images and processed images of sample B08 for eight different degrees.

Fig. 16 shows the sample images and processed images of sample B08 for eight different degrees. The sample was rotated using the triangle in the corner as a reference. With this, the reflected intensity changed as well as the positions of the holes (lighter color spot) on the surface of the sample. After the rotation, the holes in the images are located at the same spot, which implies the polarization axis is at around 135 °degrees.

Fitting parameters

As shown in Fig. 17a, $\beta^{(1)}$ is significant across the entire surface of the sample, which is an expected result because this parameter is related to the common reflection in most materials. R is slightly larger than $\beta^{(1)}$, which is consistent with Eq. (1), if $\beta_{p,v}^{(2)}\cos(2\theta)+\beta_{p,v}^{(3)}\sin(2\theta)$ is positive. In Fig. 17b, $\beta^{(2)}$ shows a significance below 5.5% across the frequency range, and is positive before 0.61 THz. $\beta^{(3)}$ shows an increasing

significance trend which reaches a maximum of 17.5% at 0.40 THz, and is negative over most of the frequency range. The coefficient of determination (CoD) r^2 plotted in Fig. 17c is above 30% over the frequency range and is higher than 58% between 0.30 THz to 0.50 THz.

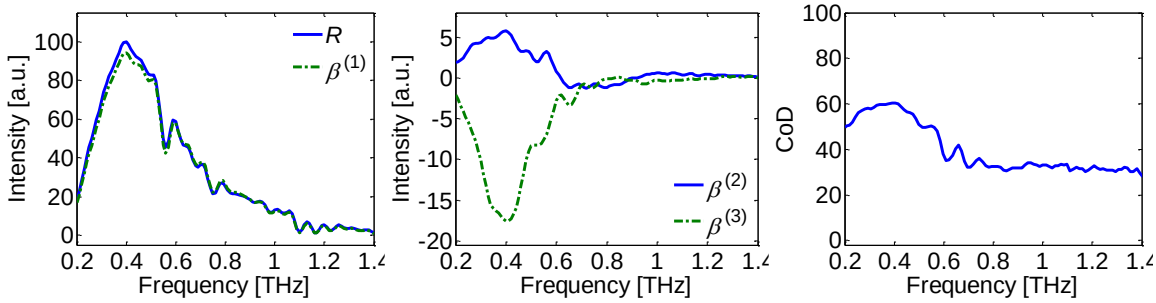

Fig. 17. Significance count for Sample B08. (a) Significance $\beta^{(1)}$ and expected reflected intensity R. (b) Significance $\beta^{(2)}$ and $\beta^{(3)}$. (c) Coefficient of determination r^2.

Reflected Intensity

The expected reflected intensity R, non-polarization reflected intensity $R^{(0)}$, and reflected polarization-dependent intensity $R^{(1)}$, are shown in Fig. 18a respectively. The reflected polarization-dependent intensity $R^{(1)}$ is about 30% between 0.30 THz to 0.50 THz. Fig. 18b shows the mean of reflected polarization intensity $R^{(2)}$ at different rotation angles. Fig. 18b also indicates the polarization axis is at 150 degrees. $R_{max}^{(2)}$ is the maximum of reflected polarization intensity $R^{(2)}$, which is at 0.40 THz. Fig. 18c shows the polarization phase, and there are abrupt phase changes at 0.61 THz and 0.90 THz.

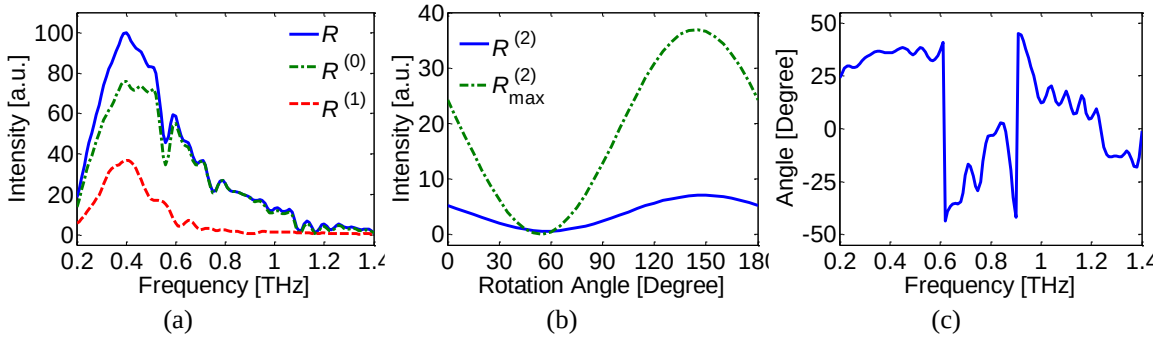

Fig. 18. Reflected intensity for Sample B08. (a) Expected reflected intensity R, non-polarization reflected intensity $R^{(0)}$, and reflected polarization-dependent intensity $R^{(1)}$, respectively. (b) Reflected polarization intensity $R^{(2)}$. The maximum of $R^{(2)}$ is at 0.40 THz. (c) Polarization phase.

E2. SAMPLE H451#8

Fitting parameters

As shown in Fig. 19a, R and $\beta^{(1)}$ are comparable. In Fig. 19b, $\beta^{(2)}$ and $\beta^{(3)}$ show a significance below 1.5% across the frequency range. The coefficient of determination (CoD) r^2 plotted in Fig. 19c is above 30% over the frequency range.

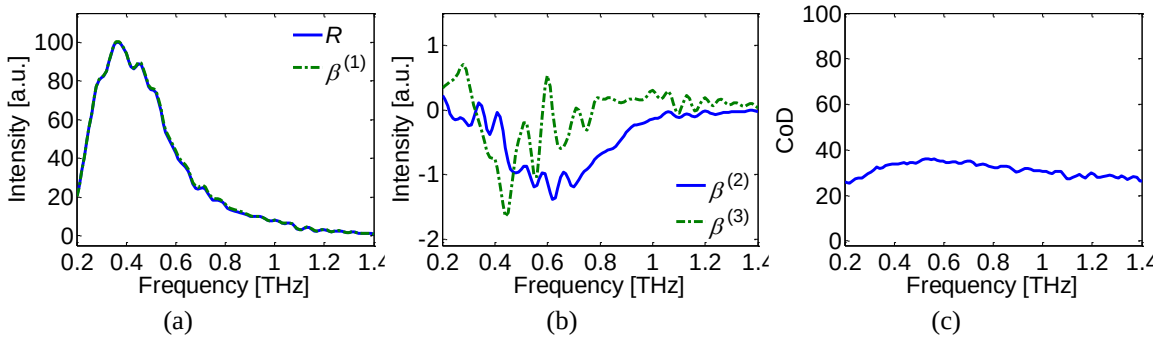

Fig. 19. Significance count for Sample H451#8. (a) Significance $\beta^{(1)}$ and expected reflected intensity R. (b) Significance $\beta^{(2)}$ and $\beta^{(3)}$. (c) Coefficient of determination r^2.

Reflected Intensity

The expected reflected intensity R, non-polarization reflected intensity $R^{(0)}$, and reflected polarization-dependent intensity $R^{(1)}$, are shown in Fig. 20a respectively. $R^{(1)}$ is about 1% in the whole frequency range, so there is hardly any polarization dependent reflection behavior. Fig. 20b shows the mean of reflected polarization intensity $R^{(2)}$ at different rotation angles. $R_{max}^{(2)}$ is the maximum of reflected polarization intensity $R^{(2)}$, which is at 0.61 THz. Fig. 20c shows the polarization phase.

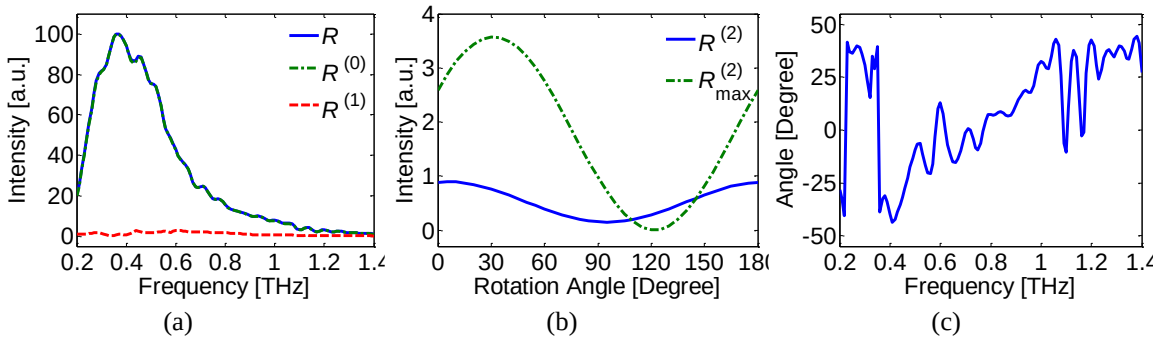

Fig. 20. Reflected intensity for Sample H451#8. (a) Expected reflected intensity R, non-polarization reflected intensity $R^{(0)}$, and reflected polarization-dependent intensity $R^{(1)}$, respectively. (b) Reflected polarization intensity $R^{(2)}$. The maximum of $R^{(2)}$ is at 0.61 THz. (c) Polarization phase.

As shown in Fig. 19b and Fig. 19b, $R_{max}^{(2)}$ of sample B08 is ten times higher than sample H-451#8 and the average is 6 times higher. H-451#8 shows nearly no polarization-dependence. This is because B08 is more porous than H-451#8 and has a larger average domain distribution, which makes it polarization-dependent. On the other hand, H-451#8 is isotropic and structurally stronger, having smaller domain distribution, so nearly no polarization-dependent reflectivity is observed. In addition, the polarization-dependent reflection is also frequency dependent, which can be a method to determine the porosity of the graphite samples.

For more results on additional graphite samples, please refer to the Additional Results section of the Appendix.

Fig. 21 shows the polarization-dependent intensities $R^{(1)}$ and the maximum polarization frequencies for samples with different densities, and the data is fitted by a third order polynomial equation. The sample with the higher density is less porous and has a smaller average domain distribution. As a consequence, it is less polarization-dependent, with limited polarization-dependent intensity. The maximum polarization frequency also increases as the sample density decreases, because higher density indicates smaller grain size and the

corresponding THz frequency is higher. In contrast, when the sample density is low, it tends to be more porous and has larger grain size, so it is more polarization dependent and the maximum polarization frequency is lower. However, the unoxidized samples, B08 and C52, do not obey this principle. Though their density is over 1700 kg/m^3, they still show highly polarization-dependent behavior.

Fig. 22 shows the polarization-dependent intensity for different samples oxidized at 600 ℃, 650 ℃ and 700 ℃. The samples oxidized at the higher temperature tend to be more polarization dependent, with the exception of sample H-451#7.

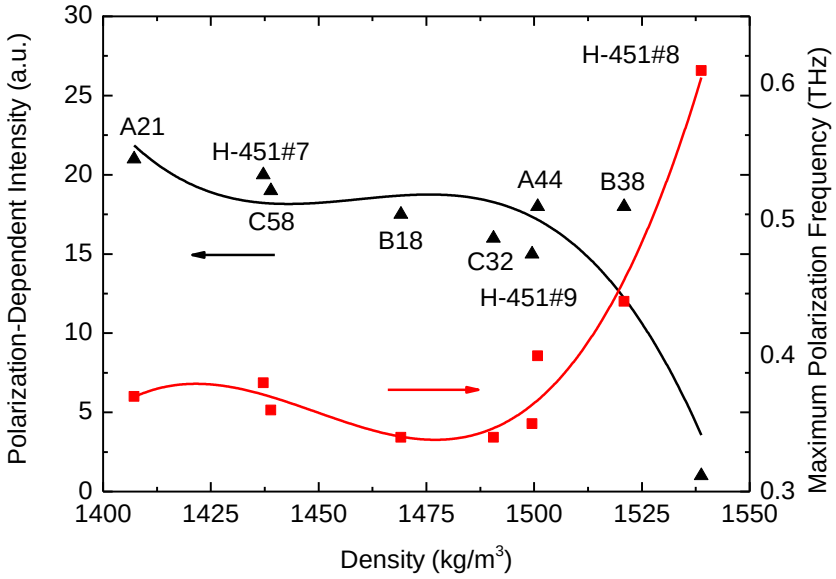

Fig. 21. The polarization-dependent intensities $R^{(1)}$ (black triangular dot) and the maximum polarization frequencies (red square dot) for samples with different densities.

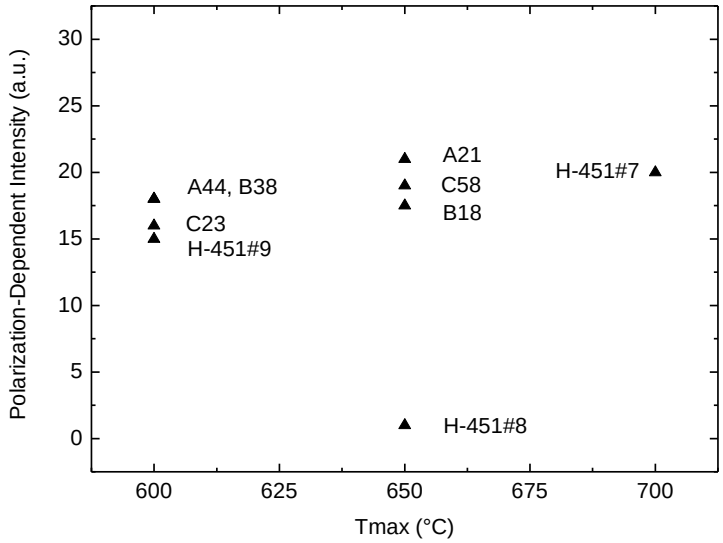

Fig. 22. The polarization-dependent intensity for different samples oxidized at 600 ℃, 650 ℃ and 700 ℃.

F. BILLET DEPENDENCE

F1. SAMPLE PCEA CENTER BILLET

Fitting parameters

As shown in Fig. 23a, R and $\beta^{(1)}$ are comparable. In Fig. 23b, $\beta^{(2)}$ shows significances below 2% across the frequency range, and $\beta^{(3)}$ is between 0 and -2%. The coefficient of determination (CoD) r^2 plotted in Fig. 23c is about 40% over the frequency range.

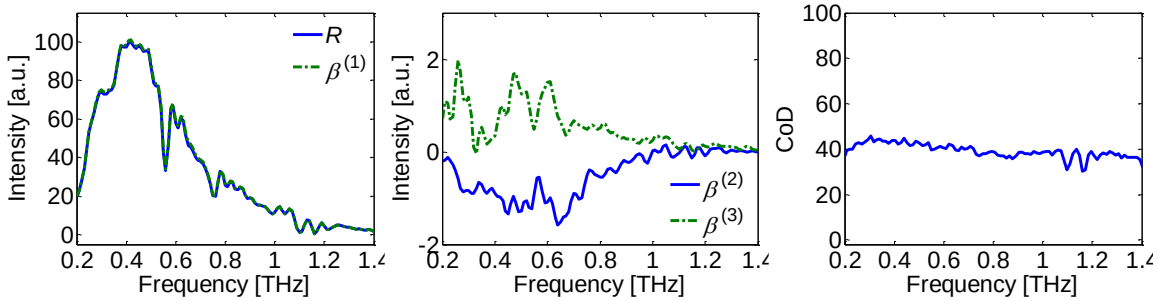

Fig. 23. Significance count for Sample PCEA central part. (a) Significance $\beta^{(1)}$ and expected reflected intensity R. (b) Significance $\beta^{(2)}$ and $\beta^{(3)}$. (c) Coefficient of determination r^2.

Reflected Intensity

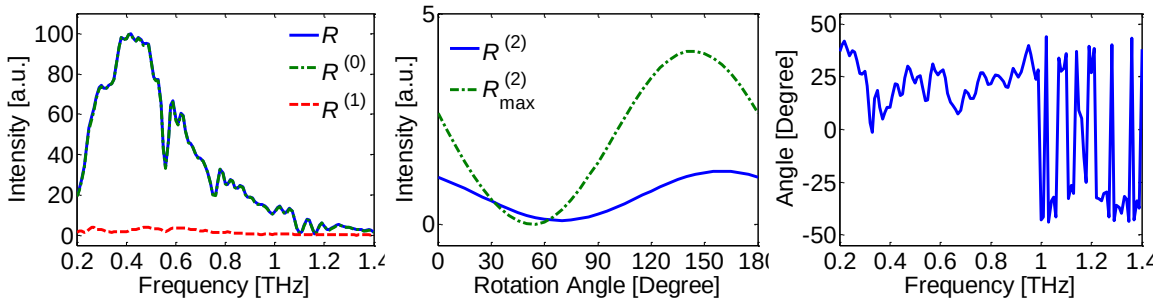

Fig. 24. Reflected intensity for Sample PCEA central part. (a) Expected reflected intensity R, non-polarization reflected intensity $R^{(0)}$, and reflected polarization-dependent intensity $R^{(1)}$, respectively. (b) Reflected polarization intensity $R^{(2)}$. The maximum of $R^{(2)}$ is at 0.39 THz. (c) Polarization phase.

The expected reflected intensity R, non-polarization reflected intensity $R^{(0)}$, and reflected polarization-dependent intensity $R^{(1)}$, are shown in Fig. 24a respectively. $R^{(1)}$ is less than 1%. Fig. 24b shows the mean of reflected polarization intensity $R^{(2)}$ at different rotation angles. Fig. 24b also indicates the polarization axis is at 148 degrees. $R_{max}^{(2)}$ is at 0.25 THz. Fig. 24c shows the polarization phase, which becomes very unstable after 1THz.

F2. SAMPLE PCEA EXTERNAL BILLET

Fitting parameters

As shown in Fig. 25a, R and $\beta^{(1)}$ are comparable. In Fig. 25b, $\beta^{(2)}$ shows a significance below 0.5% across the frequency range. $\beta^{(3)}$ shows an decreasing significance trend which reaches a minimum of -1.3% at 0.8 THz. The coefficient of determination (CoD) r^2 plotted in Fig. 25c is about 30% over the frequency range.

The expected reflected intensity R, non-polarization reflected intensity $R^{(0)}$, and reflected polarization-dependent intensity $R^{(1)}$, are shown in Fig. 26a respectively. $R^{(1)}$ is less than 1%. Fig. 26b shows the mean of reflected polarization intensity $R^{(2)}$ at different rotation angles. Fig. 26b also indicates the polarization axis is at 151 degrees. $R_{max}^{(2)}$ is the maximum of $R^{(2)}$, which is at 0.38 THz. Fig. 26c shows the polarization phase.

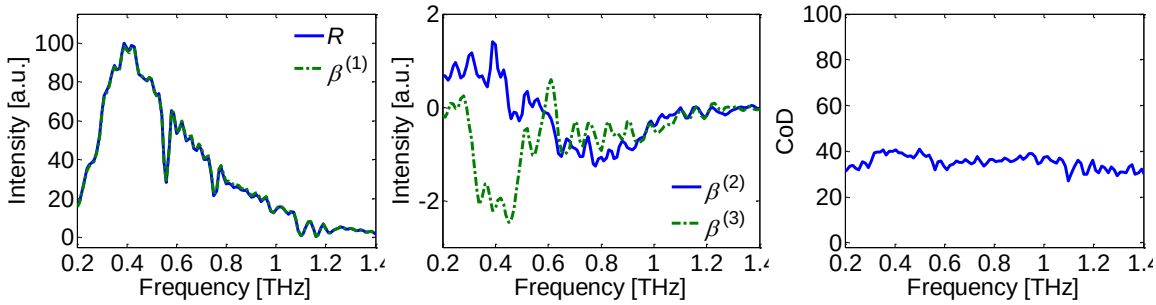

Fig. 25. Significance count for Sample PCEA external billet. (a) Significance $\beta^{(1)}$ and expected reflected intensity R. (b) Significance $\beta^{(2)}$ and $\beta^{(3)}$. (c) Coefficient of determination r^2.

Reflected Intensity

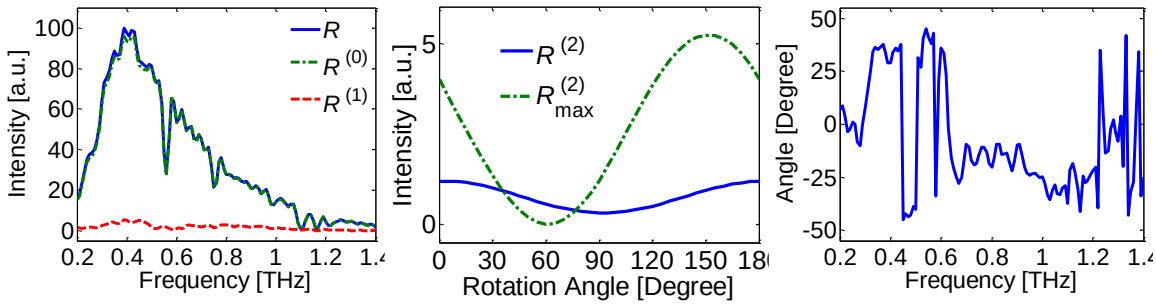

Fig. 26. Reflected intensity for Sample PCEA external billet. (a) Expected reflected intensity R, non-polarization reflected intensity $R^{(0)}$, and reflected polarization-dependent intensity $R^{(1)}$, respectively. (b) Reflected polarization intensity $R^{(2)}$. The maximum of $R^{(2)}$ is at 0.39 THz. (c) Polarization phase.

All the PCEA and IG-110 samples show little polarization dependence, because their density is higher compared to the former graphite sample. PCEA graphite from the external billet shows more polarization dependence compared to that from the center billet.

G. CONCLUSIONS

- Sample with higher density is less porous and has a smaller average domain distribution. As a consequence, it is less polarization-dependent and the maximum polarization frequency is higher.
- Samples oxidized at higher temperatures tend to be more polarization dependent.
- PCEA graphite from the external billet shows more polarization dependence compared to that from the center billet.

VII. LASER-BASED ULTRASONIC MEASUREMENTS ONOXIDIZED NUCLEAR GRADE GRAPHITE SAMPLES

Measurements were made on four types of nuclear grade graphite in September and October 2010. Sample series A is a gas-purified, molded graphite (PGXW) supplied by GrafTech International. Series B is an extruded graphite (NBG-10) supplied by SGL Carbon Group. Series C is a specialty graphite (R4-650) also supplied by SGL Carbon. Series H-451 is an extruded, medium grained, nearly isotropic graphite. See Table 1 for data on the four material types. Only samples A44, B08, C52, and H-451 #9 were tested in this round of experiments. As can be seen in Table 1, these samples were either unoxidized or thermally oxidized at 600 ℃. Measurements were also attempted on samples oxidized at 650 ℃ and 700 ℃; however, the signal to noise ratio (SNR) of the data was too low to glean any useful information.

A. RESONANT ULTRASOUND MEASUREMENTS

Experiments were run to detect any nonlinearity in the resonant response of the samples. Each sample's resonant response was measured as the sample was perturbed by a pulsed generation laser at four power levels - thermoelastic excitation, lightly ablative excitation, solidly ablative excitation, and highly ablative excitation. As the sample is driven past the thermoelastic threshold, nonlinear aspects should begin to appear in the resonant ultrasound (RUS) response. The greater incidence of physical irregularities in the material (e.g., pores, microcracks), the more significant the nonlinear component of the signal should be.

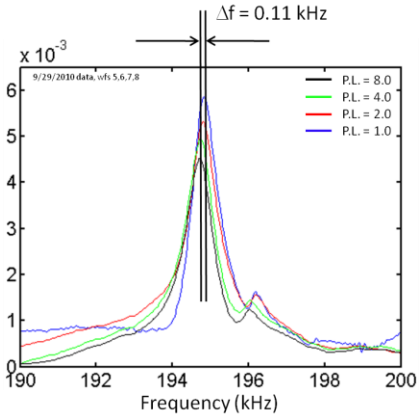

Fig. 27. Resonant peak frequency shift due to nonlinear effects induced by ablative excitation of graphite sample C-52. The frequency shifts downward 0.11 kHz from its position in the purely linear response regime.

The results from this series of test were somewhat underwhelming. A small frequency shift is seen in many of the resonant peaks; however, the magnitude of the shift is small compared to a nickel alloy sample containing extensive microcracks. See Fig. 27 for an example of the frequency shift as the generation power level is increased. In all cases, the frequency decreases as generation power increases.

A second phenomenon observed is the splitting, or lobing, of some resonant modes. Again, the incidence of this phenomenon is less common than what was observed in similar measurements made on the nickel alloy sample. See Fig. 2 for an example of this behavior. As can be seen in the figure, the frequency shift of the lobes from the fundamental peak is equal to the frequencies of the two lowest frequency peaks in the resonant spectrum.

By their very existence, those low frequency peaks raise a separate question. According to analyses based on Visscher *et al.*'s XYZ algorithm [6], the lowest frequency mode for these samples occurs at approximately 46 kHz. Nonetheless, a number of peaks is seen in the spectrum between 5 and 45 kHz. See Fig. 29. Some peaks could be electronic noise. However, the close correlation between the frequency of the peaks near 9 kHz and the frequency difference seen in Fig. 28 suggest some of those low frequency peaks are legitimate data. One possible explanation is that the sample and its holder are coupled and resonating as a single entity. Other factors being equal, a larger sample's resonant modes will occur at lower frequencies than those of a similar smaller sample.

B. SURFACE ACOUSTIC WAVE MEASUREMENTS

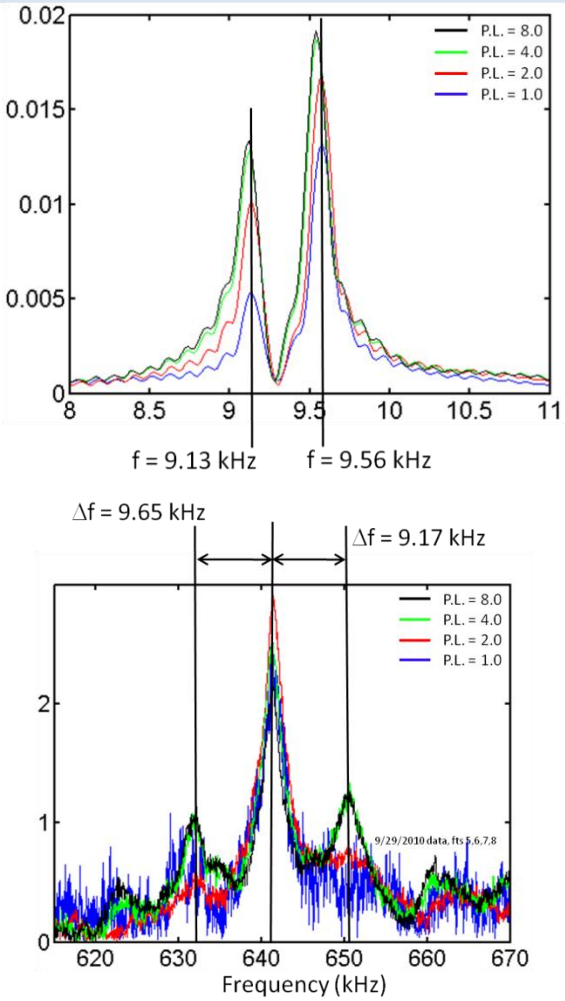

Fig. 28. Upper: The lowest frequency peaks occurring in the resonant spectrum of sample C52. Lower: Lobed resonant peak in the same spectrum. The lobes appear at higher generation powers as the sample's response becomes nonlinear. Note that the frequency deltas between the central peak and the lobes correlate to the center frequencies of the peaks at ~9 kHz.

A second set of measurements was made on the samples. In this case, surface acoustic waves (SAWs) were used to measure wave propagation speed in each sample. Measurements were taken in only one direction, so no indications of anisotropy are apparent from this data. Based on the data gathered so far, SAW measurements appear to hold more promise for characterizing graphite samples than RUS measurements.

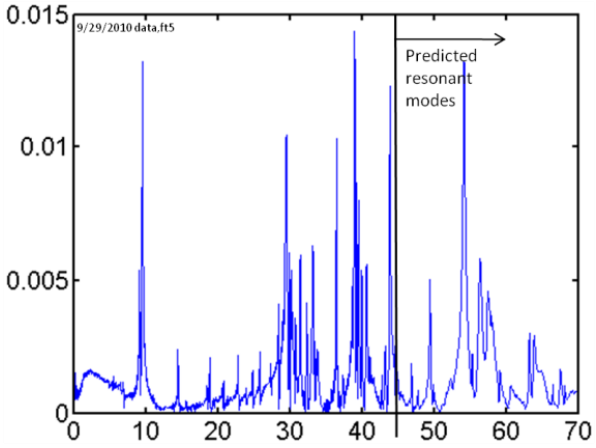

Fig. 29. The first resonant mode for sample C52 is predicted to occur at ~46 kHz. Nonetheless, a number of resonant peaks are visible in the spectrum below 45 kHz, including the pair of peaks at ~9 kHz seen in the upper pane of Fig. 2. What is the source of these seemingly extraneous peaks?

Wave propagation speeds appear to correlate with sample mass density. The denser, unoxidized samples allow SAWs to propagate more rapidly than in the samples that had already undergone oxidation. See Fig. 30. With further testing, it may be possible to demonstrate a direct link between density and porosity [10], and thus have a simple method for measuring porosity growth in oxidized samples. Further delving into the differences in the four measurements, it appears that the method of manufacture of the different samples may be a secondary factor. (Refer to Table 1) Within the two data subsets – unoxidized and oxidized – time-of-flight across the extruded samples is faster than in the molded and specialty graphite.

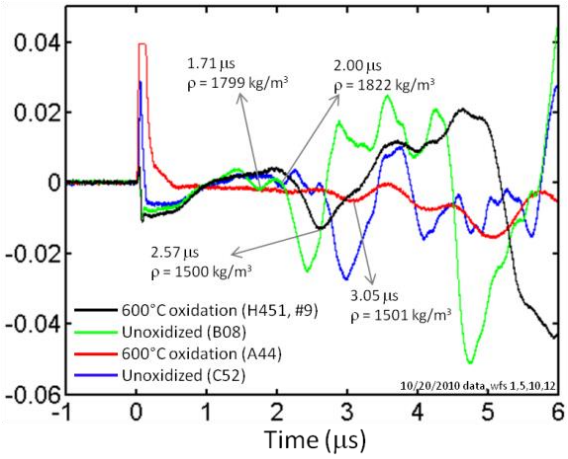

Fig. 30. SAWs recorded for each of the four samples. Propagation speed appears to correlate to density primarily, and secondarily to method of manufacture.

VIII. SUMMARY AND CONCLUSIONS

In this project, we conducted a comprehensive study on nuclear graphite properties with terahertz (THz) imaging. At first, high order pyrolytic graphite (HOPG) was characterized using both transmission and reflection THz spectroscopy in a broadband range. Two different THz time-domain spectroscopy systems were used for the characterization of the samples: a conventional THz TDS system for transmission and reflection measurement and an air-biased coherent detection (ABCD) THz spectroscopy system for reflection measurement. We defined three measurement geometries according to the different combination of THz

waves propagating direction, polarization direction and carbon layer direction. Strong birefringence is observed with different dielectric constants along three geometries. The lowest dielectric constants are obtained when THz waves propagate along the carbon plane direction and are polarized perpendicular to the plane.

In order to get the whole birefringence information of the graphite for three geometries, Graphite samples H-451#9, A44, B08 and C21 (from INL) were carefully imaged by a CW THz gas laser (SIFIR-50, Coherent Inc.) as a source and a pyroelectric sensor (PY55, Goodrich Co.) as a detector. However, the continuous wave (CW) imaging of the graphite samples indicates that the sample reflection depends on the THz polarization even if the propagation direction of the THz is not varied with respect to the carbon layer plane. The optical properties of the samples depend strongly on the complex refractive index of the material. The differences in the contrast and the features of the samples for two different orientations of the sample indicate that the material is anisotropic at THz frequencies. Furthermore, the samples from different categories show different structure and different contrast indicating that the samples have different pore size and structure.

Based on this result, we use a phase sensitive THz system again to study the graphite properties. In this exploration, various graphite samples, A21, A44, B08, B18, B38, C23, C52, C58, H-451#7, H-451#8, H-451#9, PCEA and IG-100, were studied. By imaging nuclear graphite samples in reflection mode at nine different incident polarization angles using THz time-domain-spectroscopy, we find that different domain distributions and levels of porosity will introduce polarization dependence in the THz reflectivity. A sample with a higher density is less porous and has a smaller average domain distribution. As a consequence, it is less polarization-dependent and the maximum polarization frequency is higher. The results also show that samples oxidized at higher temperatures tend to be more polarization dependent. Graphite from the external billet is more polarization dependent compared to that from the center billet. In addition, we also performed laser-based ultrasonic measurements on these graphite samples. The result shows that the denser, unoxidized samples allow surface acoustic waves to propagate more rapidly than in the samples that had already undergone oxidation. Therefore, for the oxidized samples, the denser samples show less polarization-dependence, higher polarization-dependent frequency, and allow the surface acoustic waves propagate faster.

Because polarization-dependent imaging of graphite is related to the pore size and domain distribution, it would provide us with a method to determine the structural features of the graphite as well as new criteria to qualify new graphite grades. Unlike the conventional eddy current, ultrasonic, or x-ray inspection technologies used for characterizing graphite which require local operation, THz waves can be remotely generated and detected. With the help of terahertz radiation, remote measurement of the graphite properties inside the nuclear reactor might be feasible.

IX. ACKNOWLEDGEMENT

We thank Dr. Albert Redo-Sanchez, Dr. Pengyu Han, Dr. Zheng Liu and Dr. Gurpreet Kaur for participating in this project and we also thank Dr. Jianming Dai for discussions.

X. REFERENCES

1. Windes, W., T. Burchell, and R. Bratton, *Graphite technology development plan.* PLN-2497, Rev 1, October, 2010.

2. Burchell, T.D., *Irradiation induced creep behavior of H-451 graphite.* Journal of Nuclear Materials, 2008. 381(1-2): p. 46-54.

3. Ferguson, B. and X.C. Zhang, *Materials for terahertz science and technology*. Nature Materials, 2002. 1(1): p. 26-33.

4. Matsuda, O., et al., *Coherent shear phonon generation and detection with ultrashort optical pulses.* Physical Review Letters, 2004. 93(9).

5. Migliori, A., et al., *Resonant Ultrasound Spectroscopic Techniques for Measurement of the Elastic-Moduli of Solids.* Physica B, 1993. 183(1-2): p. 1-24.

6. Visscher, W.M., et al., *On the Normal-Modes of Free-Vibration of Inhomogeneous and Anisotropic Elastic Objects.* Journal of the Acoustical Society of America, 1991. 90(4): p. 2154-2162.

7. Ledbetter, H., C. Fortunko, and P. Heyliger, *Elastic-Constants and Internal-Friction of Polycrystalline Copper*. Journal of Materials Research, 1995. 10(6): p. 1352-1353.

8. Reese, S.J., et al., *On the establishment of a method for characterization of material microstructure through laser-based resonant ultrasound spectroscopy*. Ieee Transactions on Ultrasonics Ferroelectrics and Frequency Control, 2008. 55(4): p. 770-777.

9. Dai, J., X. Xie, and X.C. Zhang, *Detection of broadband terahertz waves with a laser-induced plasma in gases.* Physical Review Letters, 2006. 97(10).

10. Matikas, T.E., P. Karpur, and S. Shamasundar, *Measurement of the dynamic elastic moduli of porous titanium aluminide compacts.* Journal of Materials Science, 1997. 32(4): p. 1099-1103.

XI. PUBLICATIONS

Jing Zhang, Xi-Cheng Zhang, Albert Redo-Sanchez, "THz Polarization-Dependent Imaging of Nuclear Graphite," poster presentation at the Frontiers in Optics (FiO) 2012/Laser Science (LS) XXVIII conference in Rochester, NY, USA, (October 2012).

XII. APPENDIX

A. ADDITIONAL RESULTS

A1. SAMPLE A21

Fitting parameters

As shown in Fig. 31a, $\beta^{(1)}$ is significant across the entire surface of the sample, which is an expected result because this parameter is related to the common reflection in most materials. R is slightly smaller than $\beta^{(1)}$, which is consistent with Eq. (1), if $\beta_{p,v}^{(2)}\cos(2\theta)+\beta_{p,v}^{(3)}\sin(2\theta)$ is negative. In Fig. 31b, $\beta^{(2)}$ shows a significance below 5.3% across the frequency range, and is negative over the frequency range. $\beta^{(3)}$ shows an increasing significance trend which reaches a maximum of 8.7% at 0.37 THz, and changes from negative to positive at 0.58 THz. The coefficient of determination (CoD) r^2 plotted in Fig. 31c is above 30% over the frequency range and is higher than 40% between 0.30 THz to 0.50 THz. From Fig. 31a, we can see that the signal is close to the noise beyond 1.40 THz, therefore, results above 1.40 THz are not trustable.

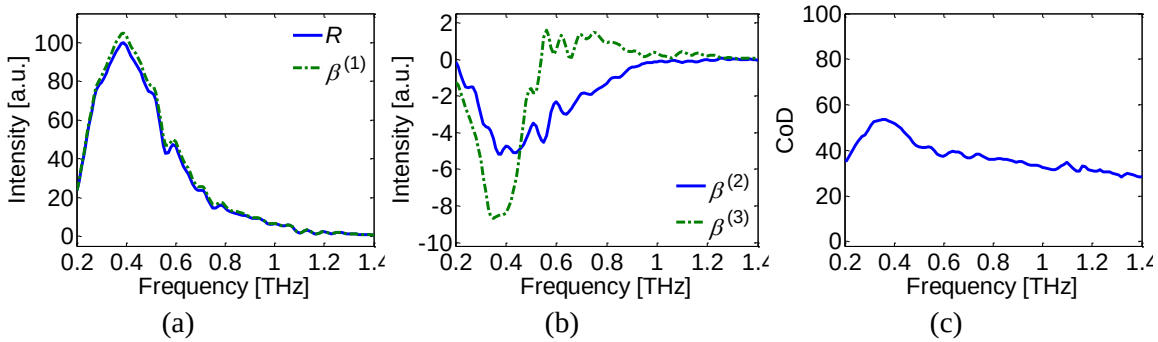

Fig. 31. Significance count for Sample A21. (a) Significance $\beta^{(1)}$ and expected reflected intensity R. (b) Significance $\beta^{(2)}$ and $\beta^{(3)}$. (c) Coefficient of determination r^2.

Reflected Intensity

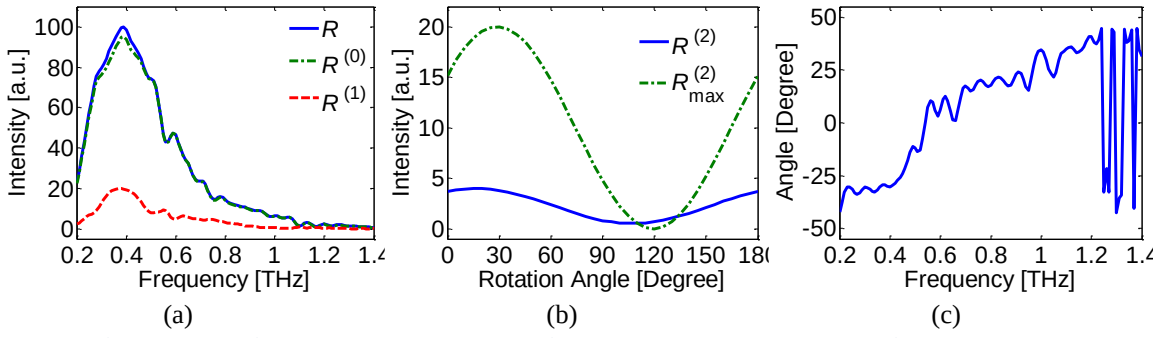

Fig. 32. Reflected intensity for Sample A21. (a) Expected reflected intensity R, non-polarization reflected intensity R(0), and reflected polarization-dependent intensity R(1), respectively. (b) Reflected polarization intensity R(2). The maximum of R(2) is at 0.37 THz. (c) Polarization phase.

A2. SAMPLE A44

Fitting parameters

As shown in Fig. 33a, $\beta^{(1)}$ is significant across the entire surface of the sample, which is an expected result because this parameter is related to the common reflection in most materials. R is slightly smaller than $\beta^{(1)}$, which is consistent with Eq. (1), if $\beta_{p,v}^{(2)}\cos(2\theta)+\beta_{p,v}^{(3)}\sin(2\theta)$ is negative. In Fig. 33b, $\beta^{(3)}$ shows a significance below 5.1% across the frequency range. After 0.58 THz, its value becomes positive. $\beta^{(2)}$ shows an increasing significance trend which reaches a maximum of 7.8% at 0.40 THz, and is negative over the frequency range. The coefficient of determination (CoD) r^2 plotted in Fig. 33c is above 30% over the frequency range and is higher than 40% between 0.30 THz to 0.50 THz.

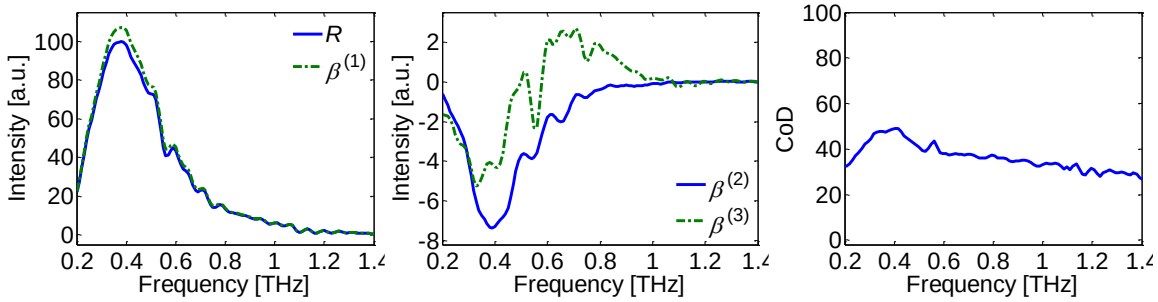

Fig. 33. Significance count for Sample A44. (a) Significance β(1) and expected reflected intensity R. (b) Significance β(2) and β(3). (c) Coefficient of determination r2.

Reflected Intensity

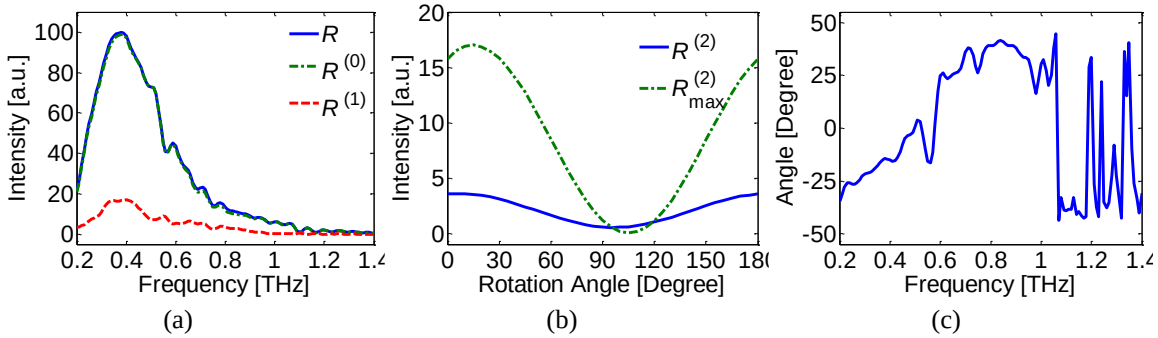

Fig. 34. Reflected intensity for Sample A44. (a) Expected reflected intensity R, non-polarization reflected intensity $R^{(0)}$, and reflected polarization-dependent intensity $R^{(1)}$, respectively. (b) Reflected polarization intensity $R^{(2)}$. The maximum of $R^{(2)}$ is at 0.40 THz. (c) Polarization phase.

The expected reflected intensity R, non-polarization reflected intensity $R^{(0)}$, and reflected polarization-dependent intensity $R^{(1)}$, are shown in Fig. 34a. The reflected polarization-dependent intensity $R^{(1)}$ is about 18% between 0.30 THz to 0.50 THz. Fig. 34b shows the mean of reflected polarization intensity $R^{(2)}$ at the whole frequency range versus different rotation angles, which fits a squared cosine function. Fig. 34b also indicates the polarization axis is at 5 degrees. $R_{max}^{(2)}$ is the maximum of reflected polarization intensity $R^{(2)}$, which is at 0.40 THz. Fig. 34c shows the polarization phase. The phase changess suddenly after 1.13 THz, which means $\beta^{(2)}$ is zero at these frequencies, indicating at these frequencies the sample shows less or little polarization dependence.

A3. SAMPLE B18

Fitting parameters

As shown in Fig. 35a, $\beta^{(1)}$ is significant across the entire surface of the sample, which is an expected result because this parameter is related to the common reflection in most materials. R is slightly larger than $\beta^{(1)}$. In Fig. 35b, $\beta^{(2)}$ shows a significance below 4.0% across the frequency range, and is positive before 0.60 THz. $\beta^{(3)}$ shows an increasing significance trend which reaches a maximum of 6.5% at 0.34 THz, and is negative over most of the frequency range. The coefficient of determination (CoD) r^2 plotted in Fig. 35c is above 30% over the frequency range.

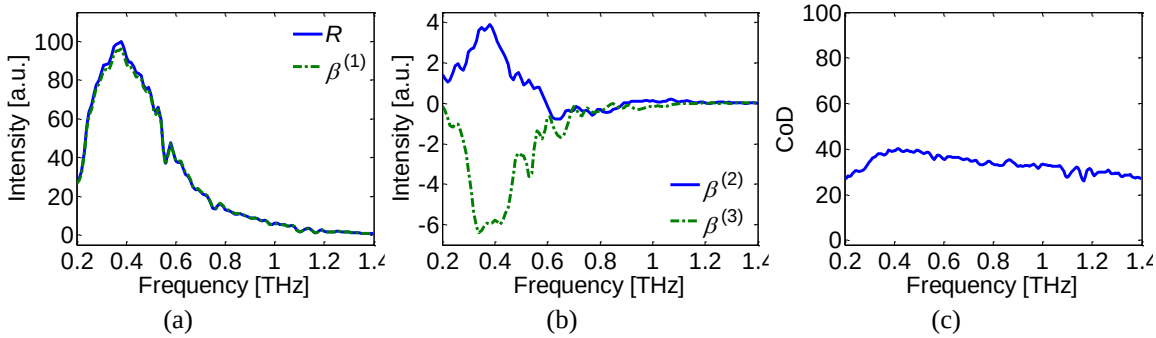

Fig. 35. Significance count for Sample B18. (a) Significance $\beta^{(1)}$ and expected reflected intensity R. (b) Significance $\beta^{(2)}$ and $\beta^{(3)}$. (c) Coefficient of determination r^2.

Reflected Intensity

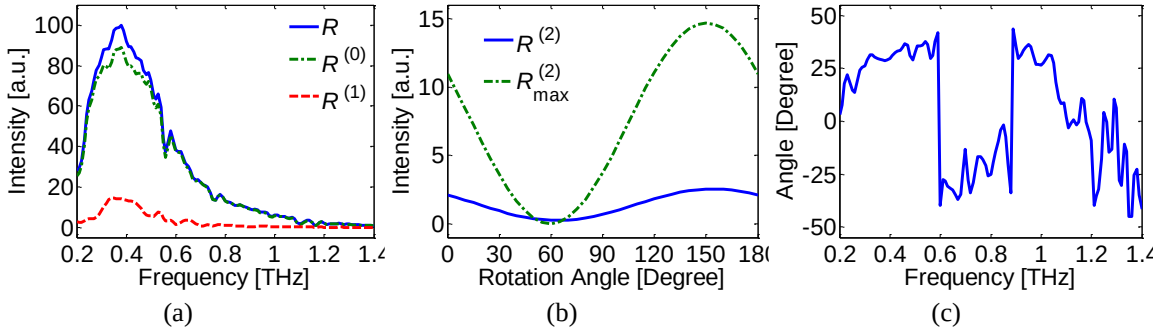

Fig. 36. Reflected intensity for Sample B18. (a) Expected reflected intensity R, non-polarization reflected intensity $R^{(0)}$, and reflected polarization-dependent intensity $R^{(1)}$, respectively. (b) Reflected polarization intensity $R^{(2)}$. The maximum of $R^{(2)}$ is at 0.34 THz. (c) Polarization phase.

The expected reflected intensity R, non-polarization reflected intensity $R^{(0)}$, and reflected polarization-dependent intensity $R^{(1)}$, are shown in Fig. 36a respectively. The reflected polarization-dependent intensity $R^{(1)}$ is about 17.5% between 0.30 THz to 0.50 THz. Fig. 36b shows the mean of reflected polarization intensity $R^{(2)}$ at different rotation angles. Fig. 36b also indicates the polarization axis is at 155 degrees. $R_{max}^{(2)}$ is the maximum of reflected polarization intensity $R^{(2)}$, which is at 0.34 THz. Fig. 36c shows the polarization phase, and there are abrupt phase changes at 0.60 THz and 0.90 THz.

A4. SAMPLE B38

Fitting parameters

As shown in Fig. 37a, $\beta^{(1)}$ is significant across the entire surface of the sample, which is an expected result because this parameter is related to the common reflection in most materials. R is slightly larger than $\beta^{(1)}$. In Fig. 37b, $\beta^{(3)}$ shows a significance below 6.5% across the frequency range, and is negative over most of the frequency range. $\beta^{(2)}$ shows an increasing significance trend which reaches a maximum of 9.2% at 0.44 THz, and is positive before 0.68 THz. The coefficient of determination (CoD) r^2 plotted in Fig. 37c is above 30% over the frequency range and is higher than 50% between 0.30 THz to 0.50 THz.

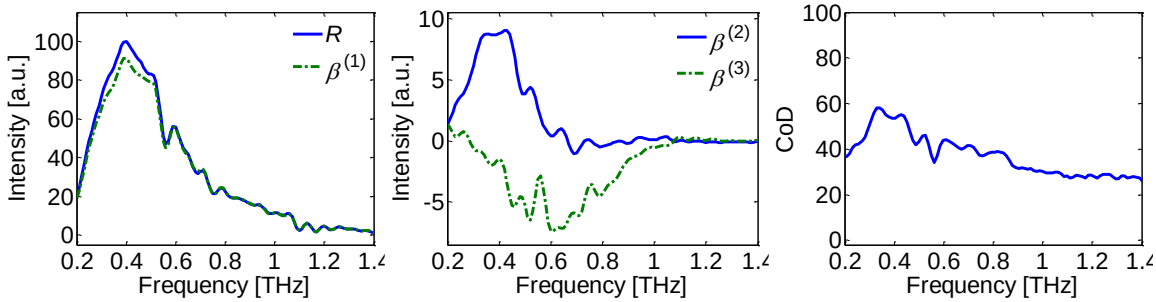

Fig. 37. Significance count for Sample B38. (a) Significance $\beta^{(1)}$ and expected reflected intensity R. (b) Significance $\beta^{(2)}$ and $\beta^{(3)}$. (c) Coefficient of determination r^2.

Reflected Intensity

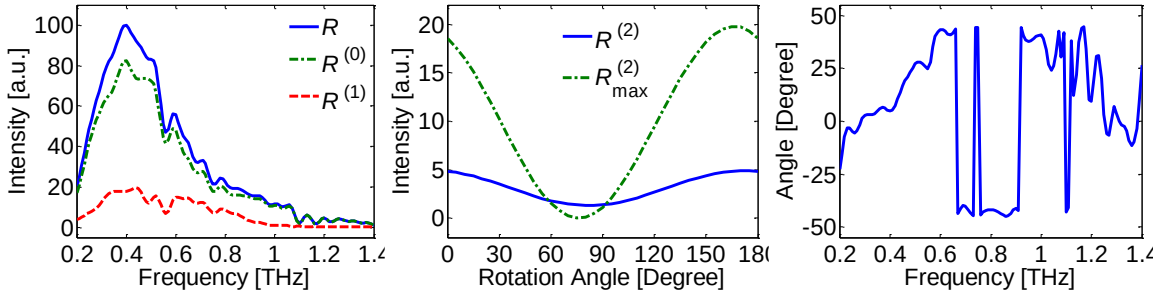

Fig. 38. Reflected intensity for Sample B38. (a) Expected reflected intensity R, non-polarization reflected intensity $R^{(0)}$, and reflected polarization-dependent intensity $R^{(1)}$, respectively. (b) Reflected polarization intensity $R^{(2)}$. The maximum of $R^{(2)}$ is at 0.44 THz. (c) Polarization phase.

The expected reflected intensity R, non-polarization reflected intensity $R^{(0)}$, and reflected polarization-dependent intensity $R^{(1)}$, are shown in Fig. 38a respectively. The reflected polarization-dependent intensity $R^{(1)}$ is about 18% between 0.30 THz to 0.50 THz. Fig. 38b shows the mean of reflected polarization intensity $R^{(2)}$ at different rotation angles. Fig. 38b also indicates the polarization axis is at 177 degrees. $R_{max}^{(2)}$ is the maximum of reflected polarization intensity $R^{(2)}$, which is at 0.44 THz. Fig. 38c shows the polarization phase, and there are abrupt phase changes at 0.68, 0. 71, 0.74 and 0.90 THz.

A5. SAMPLE C23

Fitting parameters

As shown in Fig. 39a, $\beta^{(1)}$ is significant across the entire surface of the sample, which is an expected result because this parameter is related to the common reflection in most materials. R is slightly larger than $\beta^{(1)}$, which is consistent with Eq. (1), if $\beta_{p,v}^{(2)}\cos(2\theta)+\beta_{p,v}^{(3)}\sin(2\theta)$ is positive. In Fig. 39b, $\beta^{(2)}$ shows a significance below 3.5% across the frequency range, and is positive over most the frequency range. $\beta^{(3)}$ shows an increasing significance trend which reaches a maximum of 7.0% at 0.34 THz. The coefficient of determination (CoD) r^2 plotted in Fig. 39c is above 30% over the frequency range and is higher than 40% between 0.30 THz to 0.50 THz.

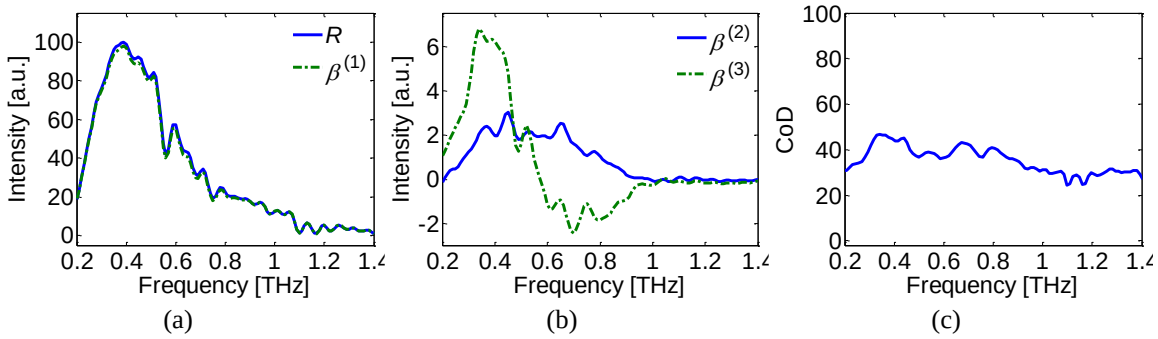

Fig. 39. Significance count for Sample C32. (a) Significance β(1) and expected reflected intensity R. (b) Significance β(2) and β(3). (c) Coefficient of determination r2.

Reflected Intensity

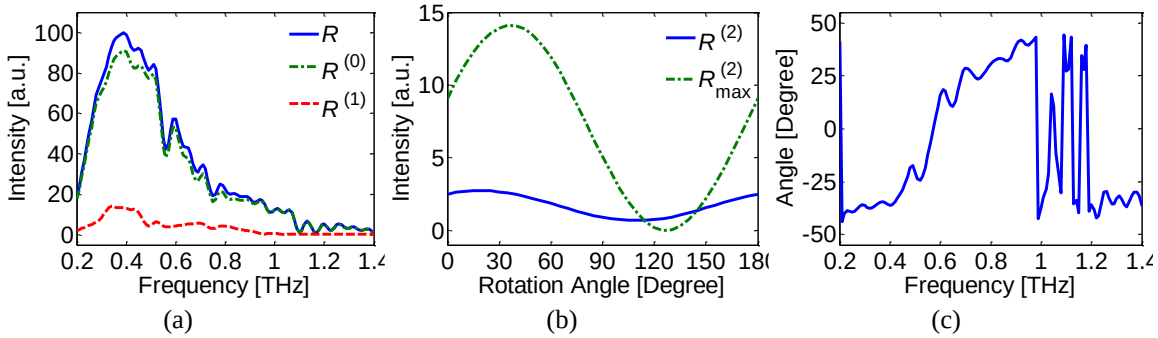

Fig. 40. Reflected intensity for Sample C32. (a) Expected reflected intensity R, non-polarization reflected intensity $R^{(0)}$, and reflected polarization-dependent intensity $R^{(1)}$, respectively. (b) Reflected polarization intensity $R^{(2)}$. The maximum of $R^{(2)}$ is at 0.34 THz. (c) Polarization phase.

The expected reflected intensity R, non-polarization reflected intensity $R^{(0)}$, and reflected polarization-dependent intensity $R^{(1)}$, are shown in Fig. 40a respectively. The reflected polarization-dependent intensity $R^{(1)}$ is about 16% between 0.30 THz to 0.50 THz. Fig. 40b shows the mean of reflected polarization intensity $R^{(2)}$ at different rotation angles. Fig. 40b also indicates the polarization axis is at 25 degrees. $R_{max}^{(2)}$ is the maximum of reflected polarization intensity $R^{(2)}$, which is at 0.34 THz. Fig. 40c shows the polarization phase, and there is an abrupt phase change after 0.99 THz.

A6. SAMPLE C52

Fitting parameters

As shown in Fig. 41a, $\beta^{(1)}$ is significant across the entire surface of the sample, which is an expected result because this parameter is related to the common reflection in most materials. R is slightly smaller than $\beta^{(1)}$. In Fig. 41b, $\beta^{(2)}$ shows a significance below 2.7% across the frequency range, and is positive over most of the frequency range. $\beta^{(3)}$ shows an increasing significance trend which reaches a maximum of 7.8% at 0.46 THz, and is positive over most of the frequency range. The coefficient of determination (CoD) r^2 plotted in Fig. 41c is above 30% over the frequency range and is higher than 40% between 0.30 THz to 0.9 THz.

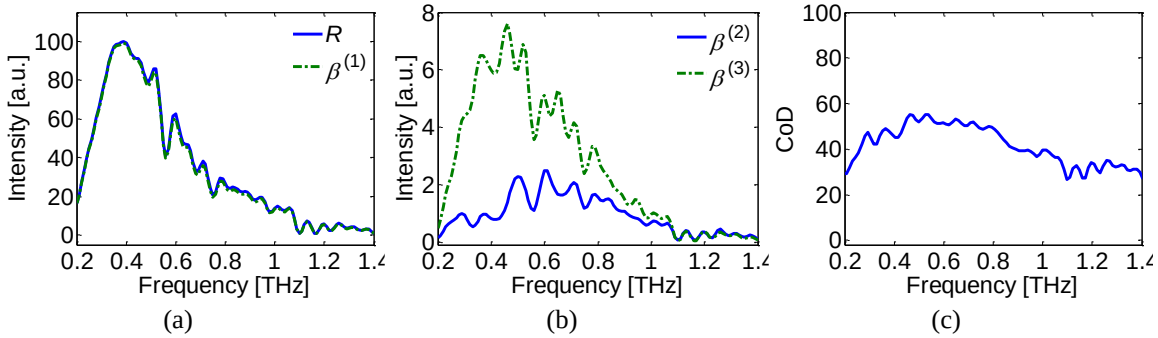

Fig. 41. Significance count for Sample C52. (a) Significance $\beta^{(1)}$ and expected reflected intensity R. (b) Significance $\beta^{(2)}$ and $\beta^{(3)}$. (c) Coefficient of determination r^2.

Reflected Intensity

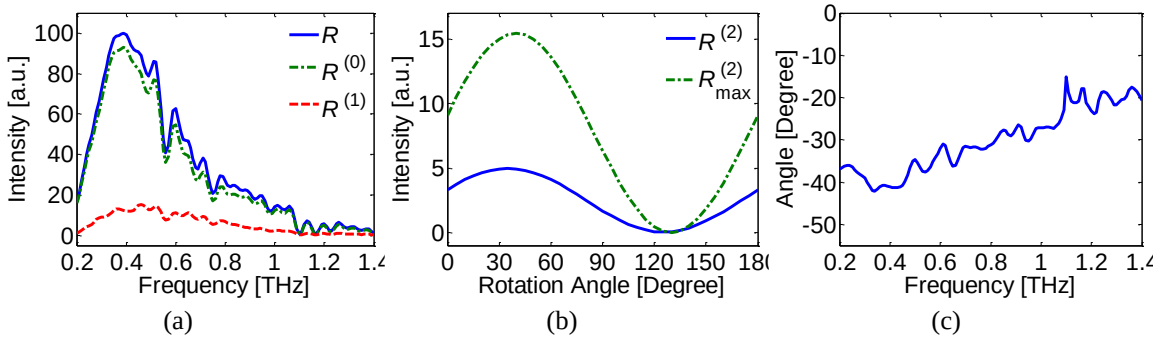

Fig. 42. Reflected intensity for Sample C52. (a) Expected reflected intensity R, non-polarization reflected intensity $R^{(0)}$, and reflected polarization-dependent intensity $R^{(1)}$, respectively. (b) Reflected polarization intensity $R^{(2)}$. The maximum of $R^{(2)}$ is at 0.46 THz. (c) Polarization phase.

The expected reflected intensity R, non-polarization reflected intensity $R^{(0)}$, and reflected polarization-dependent intensity $R^{(1)}$, are shown in Fig. 42a respectively. The reflected polarization-dependent intensity $R^{(1)}$ is about 16% between 0.30 THz to 0.50 THz. Fig. 42b shows the mean of reflected polarization intensity $R^{(2)}$ at different rotation angles. Fig. 42b also indicates the polarization axis is at 32 degrees. $R_{max}^{(2)}$ is the maximum of reflected polarization intensity $R^{(2)}$, which is at 0.46 THz. Fig. 42c shows the polarization phase, the phase is negative over the frequency range.

A7. SAMPLE C58

Fitting parameters

As shown in Fig. 43a, $\beta^{(1)}$ is significant across the entire surface of the sample, which is an expected result because this parameter is related to the common reflection in most materials. R is slightly smaller than $\beta^{(1)}$. In Fig. 43b, $\beta^{(3)}$ shows a significance below 5% across the frequency range, and is positive over most of the frequency range. $\beta^{(2)}$ shows an increasing significance trend which reaches a maximum of 10% at 0.36 THz, and is positive over most of the frequency range. The coefficient of determination (CoD) r^2 plotted in Fig. 43c is above 30% over the frequency range and is higher than 40% between 0.30 THz to 0.7 THz.

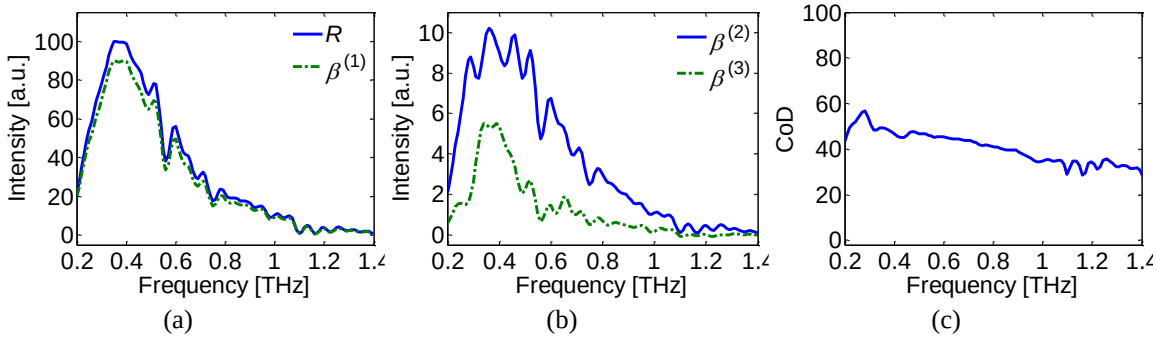

Fig. 43. Significance count for Sample C58. (a) Significance $\beta^{(1)}$ and expected reflected intensity R. (b) Significance $\beta^{(2)}$ and $\beta^{(3)}$. (c) Coefficient of determination r^2.

Reflected Intensity

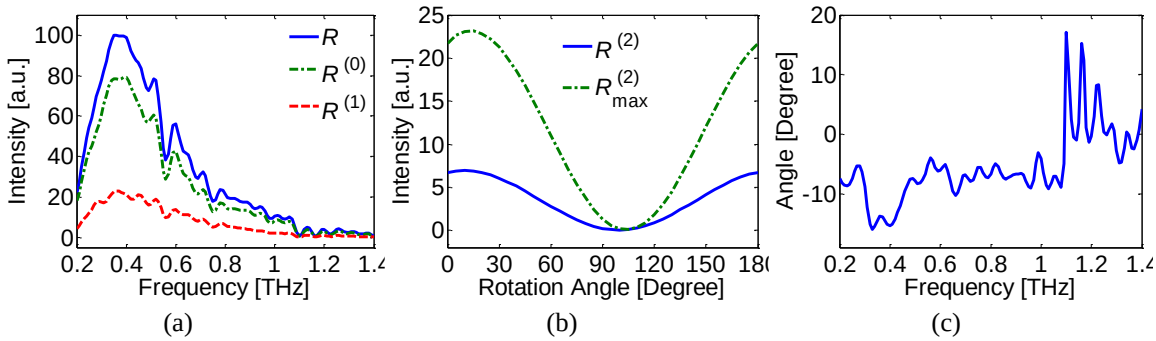

Fig. 44. Reflected intensity for Sample C58. (a) Expected reflected intensity R, non-polarization reflected intensity $R^{(0)}$, and reflected polarization-dependent intensity $R^{(1)}$, respectively. (b) Reflected polarization intensity $R^{(2)}$. The maximum of $R^{(2)}$ is at 0.36 THz. (c) Polarization phase.

The expected reflected intensity R, non-polarization reflected intensity $R^{(0)}$, and reflected polarization-dependent intensity $R^{(1)}$, are shown in Fig. 44a respectively. The reflected polarization-dependent intensity $R^{(1)}$ is about 20% between 0.30 THz to 0.50 THz. Fig. 44b shows the mean of reflected polarization intensity $R^{(2)}$ at different rotation angles. Fig. 44b also indicates the polarization axis is at 5 degrees. $R_{max}^{(2)}$ is the maximum of reflected polarization intensity $R^{(2)}$, which is at 0.36 THz. Fig. 44c shows the polarization phase.

A8. SAMPLE H451#7

Fitting parameters

As shown in Fig. 45a, $\beta^{(1)}$ is significant across the entire surface of the sample, which is an expected result because this parameter is related to the common reflection in most materials. R and $\beta^{(1)}$ are comparable. In Fig. 45b, $\beta^{(2)}$ shows a significance below 2.5% across the frequency range. $\beta^{(3)}$ shows an increasing significance trend which reaches a maximum of 16.2% at 0.38 THz. The coefficient of determination (CoD) r^2 plotted in Fig. 45c is above 30% over the frequency range and is higher than 45% between 0.30 THz to 0.50 THz.

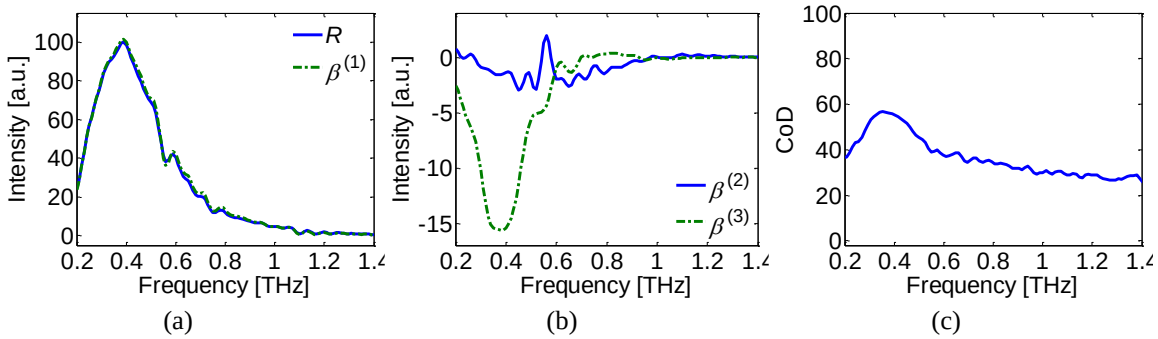

Fig. 45. Significance count for Sample H451#7. (a) Significance $\beta^{(1)}$ and expected reflected intensity R. (b) Significance $\beta^{(2)}$ and $\beta^{(3)}$. (c) Coefficient of determination r^2.

Reflected Intensity

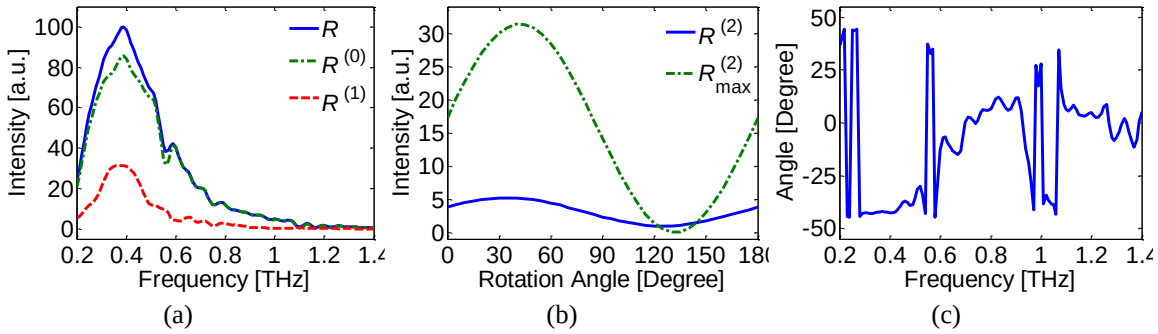

Fig. 46. Reflected intensity for Sample H451#7. (a) Expected reflected intensity R, non-polarization reflected intensity $R^{(0)}$, and reflected polarization-dependent intensity $R^{(1)}$, respectively. (b) Reflected polarization intensity $R^{(2)}$. The maximum of $R^{(2)}$ is at 0.38 THz. (c) Polarization phase.

The expected reflected intensity R, non-polarization reflected intensity $R^{(0)}$, and reflected polarization-dependent intensity $R^{(1)}$, are shown in Fig. 46a respectively. The reflected polarization-dependent intensity $R^{(1)}$ is about 30% between 0.30 THz to 0.50 THz. Fig. 46b shows the mean of reflected polarization intensity $R^{(2)}$ at different rotation angles. Fig. 46b also indicates the polarization axis is at 31 degrees. $R_{max}{}^{(2)}$ is the maximum of reflected polarization intensity $R^{(2)}$, which is at 0.38 THz. Fig. 46c shows the polarization phase.

A9. SAMPLE H451#9

Fitting parameters

As shown in Fig. 47a, $\beta^{(1)}$ is significant across the entire surface of the sample, which is an expected result because this parameter is related to the common reflection in most materials. R and $\beta^{(1)}$ are comparable. In Fig. 47b, $\beta^{(2)}$ shows a significance below 1.8% across the frequency range. $\beta^{(3)}$ shows an increasing significance trend which reaches a maximum of 6.2% at 0.35 THz. The coefficient of determination (CoD) r^2 plotted in Fig. 47c is above 30% over the frequency range.

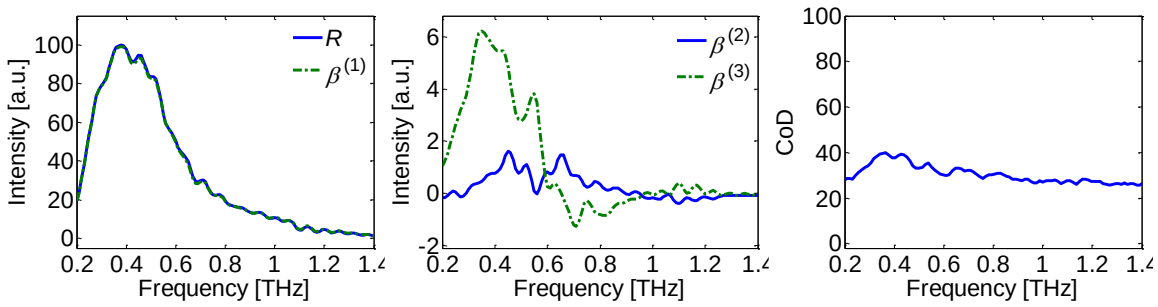

Fig. 47. Significance count for Sample H451#9. (a) Significance $\beta^{(1)}$ and expected reflected intensity R. (b) Significance $\beta^{(2)}$ and $\beta^{(3)}$. (c) Coefficient of determination r^2.

Reflected Intensity

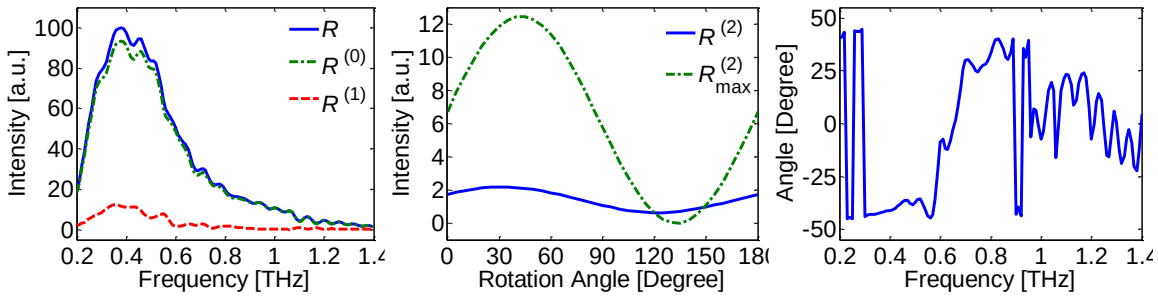

Fig. 48. Reflected intensity for Sample H451#9. (a) Expected reflected intensity R, non-polarization reflected intensity $R^{(0)}$, and reflected polarization-dependent intensity $R^{(1)}$, respectively. (b) Reflected polarization intensity $R^{(2)}$. The maximum of $R^{(2)}$ is at 0.35 THz. (c) Polarization phase.

The expected reflected intensity R, non-polarization reflected intensity $R^{(0)}$, and reflected polarization-dependent intensity $R^{(1)}$, are shown in Fig. 48a respectively. The reflected polarization-dependent intensity $R^{(1)}$ is about 15% between 0.30 THz to 0.50 THz. Fig. 48b shows the mean of reflected polarization intensity $R^{(2)}$ at different rotation angles. Fig. 48b also indicates the polarization axis is at 30 degrees. $R_{max}^{(2)}$ is the maximum of reflected polarization intensity $R^{(2)}$, which is at 0.35 THz. Fig. 48c shows the polarization phase.

A10. SAMPLE SPI-2

Fitting parameters

As shown in Fig. 49a, $\beta^{(1)}$ is significant across the entire surface of the sample, which is an expected result because this parameter is related to the common reflection in most materials. R and $\beta^{(1)}$ are comparable. In Fig. 49b, $\beta^{(2)}$ shows a significance below 1.9% across the frequency range. $\beta^{(3)}$ shows an increasing significance trend which reaches a maximum of 5.8% at 0.39 THz. The coefficient of determination (CoD) r^2 plotted in Fig. 49c is about 30% over the frequency range.

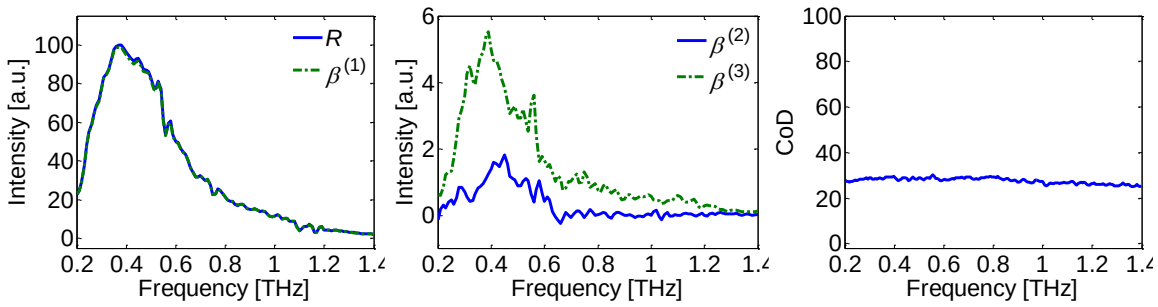

Fig. 49. Significance count for Sample SPI2. (a) Significance $\beta^{(1)}$ and expected reflected intensity R. (b) Significance $\beta^{(2)}$ and $\beta^{(3)}$. (c) Coefficient of determination r^2.

Reflected Intensity

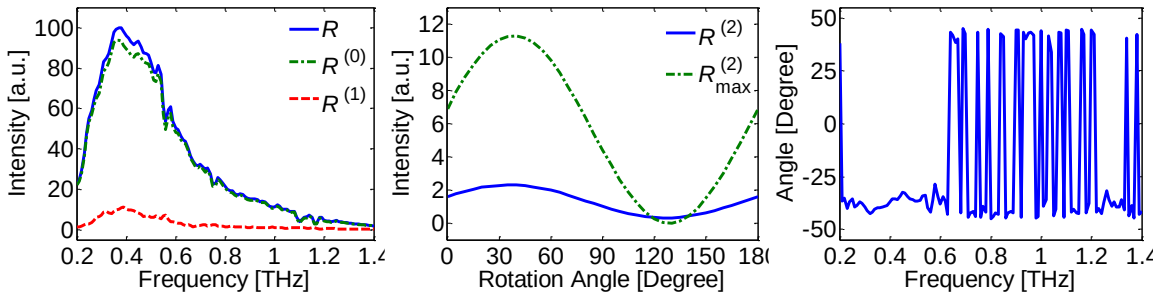

Fig. 50. Reflected intensity for Sample SPI2. (a) Expected reflected intensity R, non-polarization reflected intensity $R^{(0)}$, and reflected polarization-dependent intensity $R^{(1)}$, respectively. (b) Reflected polarization intensity $R^{(2)}$. The maximum of $R^{(2)}$ is at 0.39 THz. (c) Polarization phase.

The expected reflected intensity R, non-polarization reflected intensity $R^{(0)}$, and reflected polarization-dependent intensity $R^{(1)}$, are shown in Fig. 50a respectively. The reflected polarization-dependent intensity $R^{(1)}$ is about 10% between 0.30 THz to 0.50 THz. Fig. 50b shows the mean of reflected polarization intensity $R^{(2)}$ at different rotation angles. Fig. 50b also indicates the polarization axis is at 32 degrees. $R_{max}^{(2)}$ is the maximum of reflected polarization intensity $R^{(2)}$ at 0.39 THz. Fig. 50c shows the polarization phase, which becomes very unstable after 0.64 THz.

A11. SAMPLE IG

Fitting parameters

As shown in Fig. 51a, R and $\beta^{(1)}$ are comparable. In Fig. 51b, $\beta^{(2)}$ shows a significance below 0 in most of the frequency range. $\beta^{(3)}$ shows an significance between -3.8% and 1%. The coefficient of determination (CoD) r^2 plotted in Fig. 51c is about 36% over the frequency range.

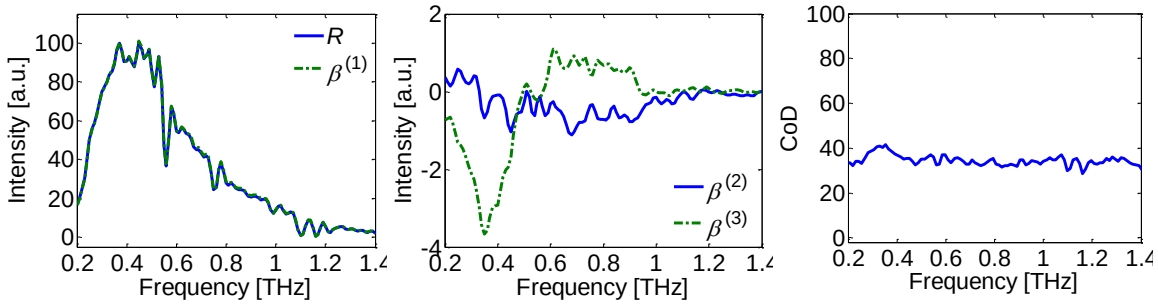

(a) (b) (c)

Fig. 51. Significance count for Sample IG-110. (a) Significance $\beta^{(1)}$ and expected reflected intensity R. (b) Significance $\beta^{(2)}$ and $\beta^{(3)}$. (c) Coefficient of determination r^2.

Reflected Intensity

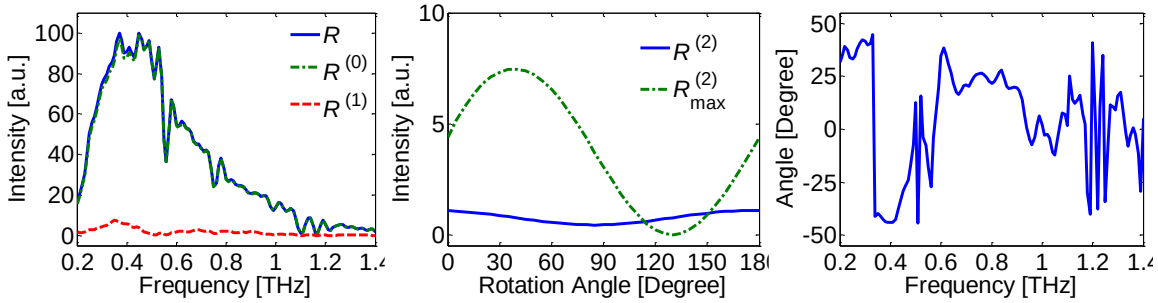

(a) (b) (c)

Fig. 52. Reflected intensity for Sample IG-110. (a) Expected reflected intensity R, non-polarization reflected intensity $R^{(0)}$, and reflected polarization-dependent intensity $R^{(1)}$, respectively. (b) Reflected polarization intensity $R^{(2)}$. The maximum of $R^{(2)}$ is at 0.39 THz. (c) Polarization phase.

The expected reflected intensity R, non-polarization reflected intensity $R^{(0)}$, and reflected polarization-dependent intensity $R^{(1)}$, are shown in Fig. 52a respectively. $R^{(1)}$ is about 2%. Fig. 52b shows the mean of $R^{(2)}$ at different rotation angles. Fig. 52b also indicates the polarization axis is at 41 degrees. $R_{max}^{(2)}$ is the maximum of $R^{(2)}$ at 0.37 THz. Fig. 52c shows the polarization phase.